



**HAL**  
open science

# Isotopic and geochemical constraints on lead and fluid sources of the Pb-Zn-Ag mineralization in the polymetallic Tighza-Jbel Aouam district (central Morocco), and relationships with the geodynamic context

Magali Rossi, Dominique Gasquet, Alain Cheilletz, Leïla Tarrieu, Hassan Bounajma, Tristan Mantoy, Laurie Reisberg, Etienne Deloule, Philippe Boulvais, Pete Burnard

## ► To cite this version:

Magali Rossi, Dominique Gasquet, Alain Cheilletz, Leïla Tarrieu, Hassan Bounajma, et al.. Isotopic and geochemical constraints on lead and fluid sources of the Pb-Zn-Ag mineralization in the polymetallic Tighza-Jbel Aouam district (central Morocco), and relationships with the geodynamic context. *Journal of African Earth Sciences*, 2017, Magmatism, metamorphism and associated mineralization in North Africa and related areas, 127, pp.194-210. 10.1016/j.jafrearsci.2016.08.011 . insu-01355138

**HAL Id: insu-01355138**

**<https://insu.hal.science/insu-01355138v1>**

Submitted on 22 Aug 2016

**HAL** is a multi-disciplinary open access archive for the deposit and dissemination of scientific research documents, whether they are published or not. The documents may come from teaching and research institutions in France or abroad, or from public or private research centers.

L'archive ouverte pluridisciplinaire **HAL**, est destinée au dépôt et à la diffusion de documents scientifiques de niveau recherche, publiés ou non, émanant des établissements d'enseignement et de recherche français ou étrangers, des laboratoires publics ou privés.

# Accepted Manuscript

Isotopic and geochemical constraints on lead and fluid sources of the Pb-Zn-Ag mineralization in the polymetallic Tighza-Jbel Aouam district (central Morocco), and relationships with the geodynamic context

Magali Rossi, Dominique Gasquet, Alain Cheilletz, Leïla Tarrieu, Hassan Bounajma, Tristan Mantoy, Laurie Reisberg, Etienne Deloule, Philippe Boulvais, Pete Burnard

PII: S1464-343X(16)30272-2

DOI: [10.1016/j.jafrearsci.2016.08.011](https://doi.org/10.1016/j.jafrearsci.2016.08.011)

Reference: AES 2648

To appear in: *Journal of African Earth Sciences*

Received Date: 24 February 2016

Revised Date: 25 July 2016

Accepted Date: 5 August 2016

Please cite this article as: Rossi, M., Gasquet, D., Cheilletz, A., Tarrieu, L., Bounajma, H., Mantoy, T., Reisberg, L., Deloule, E., Boulvais, P., Burnard, P., Isotopic and geochemical constraints on lead and fluid sources of the Pb-Zn-Ag mineralization in the polymetallic Tighza-Jbel Aouam district (central Morocco), and relationships with the geodynamic context, *Journal of African Earth Sciences* (2016), doi: [10.1016/j.jafrearsci.2016.08.011](https://doi.org/10.1016/j.jafrearsci.2016.08.011).

This is a PDF file of an unedited manuscript that has been accepted for publication. As a service to our customers we are providing this early version of the manuscript. The manuscript will undergo copyediting, typesetting, and review of the resulting proof before it is published in its final form. Please note that during the production process errors may be discovered which could affect the content, and all legal disclaimers that apply to the journal pertain.



1 **Isotopic and geochemical constraints on lead and fluid sources of the Pb-**  
 2 **Zn-Ag mineralization in the polymetallic Tighza-Jbel Aouam district**  
 3 **(Central Morocco), and relationships with the geodynamic context**

4  
 5  
 6 Magali Rossi<sup>1\*</sup>, Dominique Gasquet<sup>1</sup>, Alain Cheilletz<sup>2</sup>, Leïla Tarrieu<sup>1</sup>, Hassan Bounajma<sup>3</sup>, Tristan  
 7 Mantoy<sup>3</sup>, Laurie Reisberg<sup>4</sup>, Etienne Deloule<sup>4</sup>, Philippe Boulvais<sup>5</sup>, Pete Burnard<sup>4†</sup>

8  
 9 <sup>1</sup>Laboratoire EDYTEM, Université de Savoie-Mont Blanc, CNRS-UMR5204, Campus scientifique,  
 10 73376 Le Bourget du Lac, France

11 <sup>2</sup>Ecole Nationale Supérieure de Géologie, Laboratoire Géoressources, CNRS-UMR 7359, Université  
 12 de Lorraine, rue du Doyen Marcel Roubault, BP 40 - 54501 Vandœuvre-lès-Nancy, France

13 <sup>3</sup>Compagnie Minière de Touissit (CMT), 5 rue Ibnou Tofail, Quartier Palmiers, 20340 Casablanca,  
 14 Centre minier de Tighza, BP 114, M'irt 54450, Province de Khénifra, Morocco

15 <sup>4</sup>Centre de Recherches Pétrographiques et Géochimiques, CNRS-UMR 7358, Université de Lorraine,  
 16 BP 20, 54501, Vandœuvre-lès-Nancy, France

17 <sup>5</sup>Géosciences Rennes, Université Rennes 1, CNRS-UMR 6118, 35042 Rennes cedex, France

18  
 19 \*Corresponding author:

20 Magali Rossi, [magali.rossi@univ-smb.fr](mailto:magali.rossi@univ-smb.fr)

21  
 22 **Abstract**

23 The W-Au, Pb-Zn-Ag, and Sb-Ba mineralizations of the polymetallic Tighza-Jbel Aouam district  
 24 (central Meseta, Morocco), are hosted in Paleozoic rocks surrounding late-Carboniferous granitic  
 25 stocks. The Pb-Zn-Ag Tighza deposit formed at  $254 \pm 16$  Ma, and is clearly disconnected from the  
 26 late-Variscan W-Au deposit (295-280 Ma). The Pb-Zn-Ag mineralization precipitated from a complex  
 27 hydrothermal fluid. It displays air-normalized  $^3\text{He}/^4\text{He}$  ratio (0.018-0.103) typical of the upper crust.  
 28 This crustal component is confirmed by the oxygen and carbon isotope compositions ( $\delta^{18}\text{O} = +19$  to  
 29  $+25$  ‰;  $\delta^{13}\text{C} = -3.6$  to  $-11.2$  ‰) and the  $\epsilon_{\text{Nd}}$  values (-4.84 to -9.01) of gangue carbonates, which show  
 30 mixing of (i) fluids that have interacted with late-Carboniferous magmatic rocks, and (ii) fluids in  
 31 equilibrium with the Paleozoic metasediments. In addition, the Pb-Zn-Ag mineralization has  
 32  $^{40}\text{Ar}/^{36}\text{Ar}$  values in the range 284-315 typical of a meteoric fluid. The radiogenic Pb isotopic  
 33 compositions ( $^{207}\text{Pb}/^{204}\text{Pb} = 15.70$ - $15.80$  and  $^{206}\text{Pb}/^{204}\text{Pb} = 18.30$ - $18.50$ ) suggest leaching of Pb from  
 34 the surrounding Paleozoic metasediments and late-Variscan granites, whereas the low radiogenic  
 35 signatures ( $^{207}\text{Pb}/^{204}\text{Pb} = 15.40$  and  $^{206}\text{Pb}/^{204}\text{Pb} = 18.05$ ) provide evidence of a deeper source attributed  
 36 to the lower crust.

37 Crustal thinning related to extensional tectonics in late-Permian and Early-Triassic lead to high-K  
38 calc-alkaline to alkaline magmatic activity, which is evidenced by a dense SW-NE-trending dike  
39 network that pre-dated the Atlantic Ocean opening (early Liassic times). This magmatic event induced  
40 a regional heat flux increase that triggered the circulation of a complex hydrothermal fluid, which has  
41 a strong crustal component, but also a meteoric and a lower crustal components. The polymetallic  
42 district of Tighza-Jbel Aouam thus results from superposition of an intrusion related porphyry-gold  
43 mineralization (W-Au, 286 Ma) followed by a Pb-Zn-Ag epithermal mineralization (254 Ma), during  
44 two distinct magmatic-hydrothermal events.

45 The proposed metallogenic model for the Pb-Zn-Ag Tighza-Jbel Aouam deposit provides new  
46 constraints for the Pb-Zn-Ag exploration in the Moroccan Meseta. Exploration targets must take into  
47 account the following geological features: (i) Permo-triassic high-K calc-alkaline to alkaline dikes, (ii)  
48 extensional tectonics and reactivation of ancient crust-scale faults and shear zones, and (iii) Paleozoic  
49 series containing organic matter (e.g., black shales) subjected to low grade metamorphism (e.g.,  
50 greenschist facies).

51

52 **Keywords** : Pb-Zn-Ag deposit, Permian-Triassic extensional tectonics, Tighza-Jbel Aouam district,  
53 Central Morocco, lead and fluid sources, isotopic (O-C, Sm-Nd, Ar-He, Pb-Pb) data

54

## 55 **1. Introduction**

56 West European and Moroccan Paleozoic formations hold numerous volcanogenic massive sulphide  
57 (VMS), Mississippi Valley type (MVT), sedimentary exhalative (SEDEX) as well as vein-types Pb-  
58 Zn-Ag deposits (e.g., Arribas and Tosdal, 1994; Guilbert and Park, 1999; Marignac and Cuney, 1999;  
59 Bouabdellah et al., 2009; Subías et al., 2015, and references therein). Dating of the mineralizing events  
60 as well as characterization of the fluid and metal sources are usually difficult to obtain because of fluid  
61 mixing, secondary remobilization, and the absence of suitable minerals for dating. As vein deposits  
62 frequently occur in close association with late Variscan granites they have long been considered being  
63 genetically related to them.

64 The polymetallic Tighza-Jbel Aouam district (TJAD; central Meseta, Morocco) displays two main  
65 types of mineralization, W-Au and Pb-Zn-Ag, hosted in Paleozoic rocks surrounding late-  
66 Carboniferous high-K calc-alkaline granitic stocks (Agard et al., 1958; Cheilletz, 1984; Jébrak, 1984;  
67 Nerci, 2006; Marcoux et al., 2015; Rossi et al., 2016). It has long been considered to have a single  
68 magmatic-hydrothermal origin due to the spatial zoning of mineralization around a supposed hidden  
69 batholith (Agard et al., 1958; Desteucq, 1974). The W-Au mineralization and related potassic  
70 alteration from the “Mine Granite” are coeval and dated at  $286 \pm 0.4$  Ma (Cheilletz et Zimmermann,  
71 1982; Nerci, 2006; Watanabe, 2002). Based on field observations and isotopic studies, Agard et al.  
72 (1958), Cheilletz (1984), Jébrak (1984) and Marcoux et al. (2015) suggested that the Pb-Zn-Ag ore  
73 was emplaced after the W-Au deposit without further precision on the time gap. However, Marcoux et

74 al. (2015) consider the Pb-Zn-Ag mineralization to be the last stage of a reduced intrusion-related gold  
75 deposit, with fluid focusing at the top of the solidified and cold intrusion. The hydrothermal activity  
76 associated with the Pb-Zn-Ag deposit was recently dated at  $254 \pm 16$  Ma (Tarrieu, 2014; Cheilletz et  
77 al., 2015; Rossi et al., 2016), demonstrating the disconnection between the Pb-Zn-Ag mineralization  
78 and the W-Au mineralization. A new metallogenic model, based on the disconnection from spatially  
79 associated granites, needs to be considered for the TJAD. This model could be applied to other Pb-Zn-  
80 Ag deposits in similar geological context.

81 The source of the W-Au mineralization is strongly constrained by field geology, geochemical changes  
82 related to K-alteration, fluid inclusions analysis and Pb-Pb isotopes (Cheilletz, 1984; Nerci, 2006;  
83 Marcoux et al., 2015). However, only scarce fluid inclusion, Sr-Nd and Pb-Pb isotopic data are  
84 available for the Pb-Zn-Ag deposit (Nerci, 2006; Castorina and Masi, 2008; Marcoux et al., 2015).  
85 This paper aims to better constrain the fluid and the lead sources of the Pb-Zn-Ag mineralization, by  
86 combining rare earth elements (REE) data and C-O, Sm-Nd, Ar-He and Pb-Pb, isotopes. The isotopic  
87 signatures of gangue carbonates and galena are used as tracers of the crustal, mantellic and meteoric  
88 reservoirs. The mineralizing events are finally integrated into the late-Variscan to Permo-Triassic  
89 geodynamic framework, in order to propose an updated metallogenic model and new exploration  
90 guides.

91

## 92 **2. Geological setting and deposit geology**

### 93 *2.1. Geology of Central Morocco*

94 The Tighza-Jbel Aouam district (TJAD) belongs to the central Meseta of Morocco, which is composed  
95 of an early to middle Paleozoic basement intruded by late Carboniferous granites (Gasquet et al.,  
96 1996; Michard et al., 2008) as well as by numerous Permo-Triassic intermediate to felsic dikes  
97 (Gasquet and Bouloton, 1995) and Permian volcanic rocks (Youbi et al., 1995; Figure 1). The  
98 Paleozoic rocks are covered by Mesozoic-Cenozoic sedimentary formations. The felsic intrusive rocks  
99 are spatially associated with W, Sn, F, Sb and Pb-Zn-Ag deposits (Agard et al., 1958; Cheilletz, 1984;  
100 Jébrak, 1984; Boutaleb, 1988; Giuliani et al., 1989; Boushaba and Marignac, 2009). The Meseta  
101 domain corresponds to a complex collage of terranes representing several Variscan tectonic phases  
102 since Devonian times (Figure 1; Michard et al., 2008; Murphy et al., 2016). The main Variscan  
103 collisional events resulted in crustal thickening, folding and Variscan granite emplacement. The latest  
104 collisional phase involved NW-verging fold, duplexes and nappes (Michard et al., 2008, and  
105 references therein). Late-Carboniferous and Permian transtensive events followed, as evidenced by  
106 intra-continental basins that have been moderately deformed before the Atlasic cycle. These basins are  
107 opened by reactivation of old Variscan faults due to crustal thinning (El Hadi, 2006). The Permian  
108 sedimentary sequence is characterized by detrital sedimentation (conglomerates, sandstones and  
109 argillites) with interbedded volcanic rocks and associated dikes that crosscut the sedimentary pile  
110 (Piqué et al., 2011). Finally, the extensive tectonic regime develops during Triassic, with the opening

111 of large sedimentary basins that preceded the Atlantic Ocean opening and related CAMP activity  
112 (Mahmoudi and Bertrand, 2007; V erati et al., 2007).

113

## 114 2.2. *Geology of the Tighza-Jbel Aouam district (TJAD)*

115 The TJAD has long been known for its W-Au mineralization, as well as for major Pb-Ag-Zn and  
116 minor Sb-Ba mineralizations, hosted in Paleozoic metasediments (Agard et al., 1958; Desteucq, 1974;  
117 Cheilletz, 1984; J ebrak, 1984; Wadjiny, 1998; Nerci, 2006; Tarrieu, 2014; Marcoux et al., 2015).  
118 Upper Visean (Mississippian) limestones and schists unconformably overlie Ordovician siliceous  
119 schists and quartzites, Silurian black shales, and Devonian siliceous limestones. These Paleozoic  
120 metasediments are deformed into a succession of SW-NE-trending anticlines and synclines, and are  
121 metamorphosed up to greenschist facies. The TJAD is localized between two crustal-scale E-W shear  
122 zones that controlled the opening of tension veins and dikes during late and post-Variscan time  
123 (Figures 1 and 2).

124 The Paleozoic formations are crosscut by microgranite and micogranodiorite dikes, and by four  
125 monzogranite stocks named, from South to North, Kaolin, Mine, Mispickel, and Tighza peaks. The  
126 high-K calc-alkaline signature of all of these intrusive bodies is observed in most Moroccan Variscan  
127 granites and reflects either an enriched mantle or a lower crustal component (Gasquet et al., 1996; El  
128 Hadi et al., 2006). The monzogranite stocks have been dated at 320-300 Ma by Tarrieu (2014) and  
129 Rossi et al. (2016). The three southernmost stocks are surrounded by a large and well-delimited biotitic  
130 alteration halo related to the W-Au mineralizing event (Figure 2; Cheilletz, 1984; Cheilletz and Isnard,  
131 1985). The gravimetric study of El Dursi (2009), carried out on the TJAD, suggests that this  
132 hydrothermal alteration halo is associated with a hidden thin and shallow intrusive pluton. The W-Au  
133 mineralization thus results from a second magmatic stage at 295-280 Ma. It can be considered as a  
134 porphyry-type deposit based on (i) the genetic link with calc-alkaline magmatic activity (Cheilletz,  
135 1984; Marcoux et al., 2015), (ii) potassic alteration related to a hidden pluton (Cheilletz and  
136 Zimmermann, 1982; Cheilletz, 1984), (iii) high temperature hydrothermal fluids that have a magmatic  
137 signature (Nerci, 2006; Marcoux et al., 2015), and (iv) the occurrence of disseminations, W-rich  
138 skarns, stockworks, sheeted veins and large veins. The large E-W-trending veins formed during a  
139 dextral transpressive regime (Cheilletz, 1984).

140 The currently mined Pb-Zn-Ag mineralization, which crosscuts the W-Au ore (Figure 3), has been  
141 dated at  $254 \pm 16$  Ma (Tarrieu, 2014; Cheilletz et al., 2015; Rossi et al., 2016). It developed during a  
142 magmatic-hydrothermal episode associated with emplacement of a dense network of late-Permian  
143 dikes, found throughout the Moroccan Meseta (Bouloton and Gasquet, 1995; Gasquet and Bouloton,  
144 1995; Rossi et al., 2016). The Pb-Zn-Ag mineralization is filling NE-SW transtensive tension-gashes  
145 that developed during a NW-SE compression. The old dextral E-W shear zones are reactivated with a  
146 sinistral component during this tectonic event. Fluid inclusions analyses and calculated isochores

147 allowed Nerci (2006) and Marcoux et al. (2015) to constrain minimum trapping P-T conditions (see  
148 2.3.).

149 The polymetallic TJAD thus results from two successive magmatic-hydrothermal events that produced  
150 first the W-Au mineralization followed by the Pb-Zn-Ag mineralization (Tarrieu, 2014; Rossi et al.,  
151 2016).

152

### 153 *2.3. Geology of the Pb-Zn-Ag mineralization*

154 The Pb-Zn-Ag mineralization has been mined since 1930 from several large extensional veins with  
155 N25°E to N75°E orientations (Figure 2). In most cases, the veins display a “Y” shape, showing a  
156 connection between two veins, which suggest fracture opening as part of a conjugate strike-slip fault  
157 system (see Cheilletz 1984 for details; Figure 2). The main Pb-Zn-Ag veins are, from North to South:  
158 Filons Parallèles and Filon Nord, Filon Signal and Structure 18, Structure II, Sidi Ahmed, Ighrem  
159 Aousser and Iguer Oujna. Only Filon Signal, Structure 18, Sidi Ahmed and Ighrem Aousser are  
160 currently being mined, allowing extensive observations and sampling of fresh rocks.

161 The Pb-Zn-Ag mineralization comprises sulphides (galena + sphalerite) in a gangue of carbonates  
162 (calcite ± siderite and ankerite) ± quartz (or red chalcedony). Development of the deposit was  
163 associated with weak carbonate alteration of the Paleozoic country rocks. Analyses of fluid inclusions  
164 trapped in calcite from Sidi Ahmed vein indicate that the Pb-Zn-Ag mineralization formed at a  
165 minimum temperature of 230°C, from Na-Ca brines and a complex fluid with organic compound.  
166 Calculated isochores indicate hydrostatic pressures of at least 30 MPa (Nerci, 2006; Marcoux et al.,  
167 2015).

168 The paragenetic sequences are slightly different among the different veins. In Filon Signal and  
169 Structure 18, the mineralization is typically banded and rather symmetrical: vein minerals grew from  
170 the edge of the vein towards its center (Figure 4). These large veins display a succession of four  
171 paragenetic assemblages (Figure 4 and Figure 5): (P1) quartz + siderite, (P2) galena + calcite ±  
172 sphalerite, (P3) galena + sphalerite + siderite, and (P4) calcite + quartz + pyrite. As shown in Figure 4,  
173 the early barren P1 assemblage is not present everywhere. The Pb-Zn-Ag mineralization is associated  
174 with P2 and P3 assemblages (Figure 4 and 5). The latest hydrothermal phase (P4) is barren.

175 In Sidi Ahmed and Ighrem Aousser, the four hydrothermal successive events (pulses) display slightly  
176 different paragenetic assemblages than in Filon Signal and Structure 18 (Tarrieu, 2014; Rossi et al.,  
177 2016, Figure 5): (P1) hydraulic fracturing and precipitation of siderite + quartz, (P2) banded galena +  
178 ankerite ± sphalerite, (P3) brecciation and precipitation of galena + sphalerite, and (P4) calcite +  
179 quartz + pyrite. Jébrak (1984, 1985) noted that gangue carbonates are REE-rich.

180

### 181 **3. Sampling and analytical methods**

182 In order to provide insights into the lead and mineralizing fluid sources of the Pb-Zn-Ag  
183 mineralization, various complementary isotopic studies have been performed on sulphide minerals

184 (He-Ar on pyrite and sphalerite, Pb isotopes on galena) and on gangue siderite, ankerite and calcite  
185 (O-C isotopes, Sm-Nd, REE content). Most samples were collected within the three main Pb-Zn-Ag  
186 veins, Filon Signal, Sidi Ahmed and Ighrem Aousser veins. They were collected underground in order  
187 to provide unweathered rocks. Some additional samples were also collected from drill cores from  
188 Filon Nord and Filons Parallèles, i.e., from the northernmost veins (Figure 2).

189

### 190 3.1. REE content of carbonates

191 Four siderite (P1), six ankerite (P2) and thirteen calcite (P4) concentrates sampled in the various Pb-  
192 Zn-Ag veins were analyzed by ICP-MS at the SARM-CRPG in Nancy, France. The minerals were  
193 concentrated by handpicking. The analytical results are presented in Table 1 and Figures 6 and 7.

194

### 195 3.2. Stable isotopes (O, C)

196 Carbon and oxygen isotope analyses were carried out at the stable isotope laboratory of Géosciences  
197 Rennes (France). Analyses were performed on separated siderite, ankerite and calcite crystals sampled  
198 in Signal, Sidi Ahmed and Ighrem Aousser veins. Carbonate materials were reacted with anhydrous  
199  $\text{H}_3\text{PO}_4$  at 50°C during fifteen hours. Isotopic measurements on the liberated  $\text{CO}_2$  were made using a  
200 VG SIRA-10 triple collector mass spectrometer. Isotopic compositions are quoted using the  $\delta$  notation  
201 with respect to SMOW for  $\delta^{18}\text{O}$  and PDB for  $\delta^{13}\text{C}$ . Measured carbonate  $\delta^{18}\text{O} - \delta^{13}\text{C}$  values have been  
202 corrected using the NBS19 international and Prolabo Rennes in-house standards values. Analytical  
203 precisions are estimated to be  $\pm 0.1\text{‰}$  and  $\pm 0.15\text{‰}$  respectively for the  $\delta^{13}\text{C}$  and  $\delta^{18}\text{O}$  in carbonates.  
204 Results are presented in Table 2 and Figure 9.

205

### 206 3.3. Sm-Nd

207 In order to complete the data obtained by Castorina and Masi (2008) on siderites from Signal and Sidi  
208 Ahmed, Sm and Nd isotope analyses were performed in CRPG Nancy on ankerite and calcite from  
209 from Sidi Ahmed and Ighrem Aousser. After addition of a mixed  $^{150}\text{Nd}$ - $^{147}\text{Sm}$  spike, samples were  
210 digested in  $\text{HF} + \text{HNO}_3$ , and Sm and Nd were extracted by chromatographic techniques adapted after  
211 those of Pin et al. (1997) using TRU spec and LN spec resins. Sm and Nd isotopic compositions were  
212 determined by MC-ICP-MS (Neptune). During the period of analysis the JNdi-1 Nd standard yielded  
213  $0.512095 \pm 0.000014$  ( $2\sigma$ , 11 analyses) Analytical blanks represented  $<1\%$  of the total amount of Nd  
214 analyzed in all cases and are thus negligible. Results are reported in Table 3 and Figure 10.

215

### 216 3.4. Rare gases Ar-He

217 Sulphides from the W-Au (2 As-pyrite and 1 pyrite) and Pb-Zn-Ag mineralization (2 pyrites and 1  
218 sphalerite from Sidi Ahmed) were carefully selected under a binocular microscope to eliminate  
219 alteration and inclusions, and then crushed. The analyses were performed by P. Burnard at the CRPG  
220 -CNRS (Nancy, France) following the analytical procedure of Marty and Zimmermann (1999). The



221 amounts and the isotopic ratios of helium and argon were analyzed with a VG 5400 rare gas mass  
 222 spectrometer. Results are reported in Table 4 and Figure 11.

223

### 224 3.5. Lead isotopes

225 Six ore samples were selected from the three main veins for in-situ Pb isotope analysis on galena ( $n_{gn}$ )  
 226 and sphalerite ( $n_{sph}$ ) individual grains. 32 galena and 32 sphalerite crystals were analysed from Signal  
 227 vein:  $n_{gn} = 3$  and  $n_{sph} = 12$  in Tz10/39;  $n_{gn} = 25$  and  $n_{sph} = 10$  in Tz11/42;  $n_{gn} = 4$  and  $n_{sph} = 20$  in  
 228 Tz10/43). 7 galena crystals were analysed in sample Tz10/35 from Sidi Ahmed vein. 8 galena and 11  
 229 sphalerite crystals were analysed from Ighrem Aousser vein:  $n_{gn} = 5$  in Tz10/30;  $n_{gn} = 3$  and  $n_{sph} = 112$   
 230 in Tz10/31. Measurements were performed in CRPG-CNRS (Nancy, France) by ion microprobe  
 231 following Deloule et al. (1986), using the Cameca IMS 3F for Tz10/30 at a mass resolution of 800,  
 232 and the Cameca IMS 1270 in monocollection mode to a mass resolution of 4000 for the other samples.  
 233 All data are reported in Table 5 and Figure 12.

234

## 235 4. Results and interpretation

### 236 4.1. REE content of carbonates

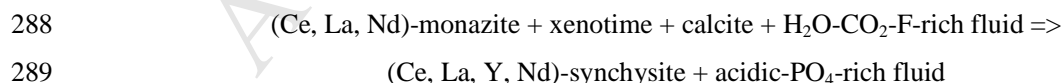
237 The total REE content of siderite, ankerite and calcite from the Tighza Pb-Zn-Ag veins ranges  
 238 between 45 and 4041 ppm ( $n=44$ , Figure 6 and Table 1; Jébrak, 1985; Castorina and Masi, 2008; this  
 239 study). About 50% of the analysed carbonates have rather low total REE content ( $< 300$  ppm), but 14  
 240 samples are significantly REE-rich and contain more than 900 ppm REE (up to 4000 ppm). Such  
 241 content is unrelated to the mineralogy or to the paragenetic stages considering that the most enriched  
 242 carbonates are a P2-ankerite (4041 ppm) and a P4-calcite (2702 ppm) in Ighrem Aousser, a P3-siderite  
 243 crystal in Sidi Ahmed (2385 ppm; Castorina and Masi, 2008), and a P2-ankerite crystal in Signal vein  
 244 (2400 to 2700 ppm; Jébrak, 1985). Changes in REE content might reflect changes in growth or fluid  
 245 flow rates (Möller et al., 1991) or changes in temperature (Möller et al., 2004). As P4-calcite crystals  
 246 cover a large REE range within a single vein, this scatter is unlikely due to variation of the fluid  
 247 temperature but rather to changes in fluid-flow rates, thus on fluid-rock ratios, depending on variable  
 248 degrees of vein opening.

249 PAAS-normalized REE+Y patterns of gangue carbonates allow identification of two distinct groups.  
 250 Most carbonates from the Signal, Sidi Ahmed and Ighrem Aousser lodes have similar PAAS-  
 251 normalized REE+Y patterns (Group 1), characterized by  $(La/Sm)_N$  lower than 1 (0.06 to 0.60),  
 252  $(Gd/Lu)_N$  higher than 1 (1.25 to 13.52), and positive  $Eu_N$  anomalies (1.5 to 3.0; Figure 7, Table 1).  
 253 Whatever the vein, the carbonate (siderite, ankerite or calcite) or the paragenetic sequence, all  
 254 carbonates from group 1 display similar REE+Y patterns, suggesting that they crystallized from a  
 255 unique hydrothermal fluid. The various paragenetic sequences reflect the evolution of the reactive  
 256 fluid composition due to fluid-rock interaction. Regardless of mineralogy and paragenetic sequences,  
 257 half of group 1 carbonates have  $(La/Lu)_N$  lower than 1 (0.1 to 1.0), and half have  $(La/Lu)_N$  higher than

258 1 (1.0 to 5.6). Different pH conditions (Castorina and Masi, 2008) or changes in temperature could  
 259 explain these differences. The upward-convex shape REE+Y patterns are typical of hydrothermal  
 260 fluids and carbonates that precipitated from hydrothermal crustal fluids in various geological contexts  
 261 (e.g., Michard, 1989; Lüders et al., 1993; Hecht et al., 1999; Torres-Ruiz 2006, Margoum et al., 2015,  
 262 and references therein). Therefore, the REE+Y patterns of gangue carbonates are representative of the  
 263 hydrothermal fluid, so that it not possible to discriminate among the possible crustal sources of REE  
 264 (local sedimentary and magmatic host-rocks, or other crustal sources) based on REE+Y patterns only.  
 265 As already discussed by Castorina and Masi (2008), the slight negative Ce<sub>N</sub> anomaly, which is typical  
 266 of marine carbonate, likely reflect fluid-carbonate interaction or a slight contribution of seawater. The  
 267 positive Eu<sub>N</sub> anomalies could either reflect (i) REE mobilization at high-temperature, and precipitation  
 268 at lower temperature (> 200-250°C) under reducing and mildly acidic conditions (Bau 1991; Bau and  
 269 Möller, 1992), (ii) inheritance from host-rock alteration, or (iii) chemical complexation reactions or  
 270 sorption effects. As fluid inclusions indicate that the Pb-Zn-Ag mineralization precipitated at a  
 271 minimum temperature of 230°C (Nerci, 2006; Marcoux et al., 2015), the observed positive Eu<sub>N</sub>  
 272 anomalies most likely result from temperature conditions of REE mobilization and precipitation (Bau  
 273 1991; Bau and Möller, 1992). Finally, the hydrothermal fluid probably has interacted with upper  
 274 crustal rocks and marine carbonates, under rather high temperatures in order to mobilize REE+Y, and  
 275 then precipitated at temperature higher than 230°C.

276 Two P4-calcite crystals sampled in late-calcite veins show different PAAS-normalized REE+Y  
 277 patterns (Group 2), with (La/Sm)<sub>N</sub> lower than 1 (0.33 and 0.45), (Gd/Lu)<sub>N</sub> lower than 1 (0.32 and 0.61),  
 278 and negative Eu anomalies (0.46 and 0.59; Figure 11). The HREE enrichment, as well as the strong  
 279 positive Y<sub>N</sub> anomalies are similar to those found in marine carbonates (Hu et al., 1988; Nothdurft et al.,  
 280 2004), suggesting these two calcites might have precipitated either from a fluid with a rather strong  
 281 seawater component, or that interacted mostly with marine carbonates.

282 The high REE content of gangue carbonates results from microscopic solid inclusions of REE-rich  
 283 minerals evidenced from SEM observation (Figure 8). More than 95% of the analyzed REE-rich  
 284 crystals are La-rich synchysite (i.e., Ce-Y-Nd-La-bearing fluorocarbonate; Figure 8). Destabilisation  
 285 reaction of rare xenotime and monazite into synchysite has been observed (Tarrieu, 2014), suggesting  
 286 that at least some of the synchysite crystals are secondary phases. The mineralogical reaction follows  
 287 the equation:



290 According to this equation, circulation of a H<sub>2</sub>O-CO<sub>2</sub>-F-rich fluid is required, and REE+Y remain  
 291 immobile. The occurrence of these REE-bearing minerals explains most of the total REE content of  
 292 gangue carbonates. Indeed, Ce accounts for 24 to 40 % of the total REE content of carbonates, Nd for  
 293 about 20 % and La for 5 to 20 %. Yttrium is also quite abundant and represents 15 to 25 % of total

294 REE+Y content (Table 1). Such Ce:La:Nd:Y ratios are in the same range than in the synchysite  
295 composition.

296 In the TJAD, the high REE contents of gangue carbonates from the Pb-Zn-Ag mineralization is mainly  
297 due to the occurrence of abundant solid inclusions of (Ce, La, Y, Nd)-rich synchysite micro-crystals  
298 that precipitated from the hydrothermal fluid.

299

#### 300 4.2. Stable isotopes (O, C)

301 No systematic difference between the stages of carbonation is evidenced from table 2, regardless the  
302 nature of the gangue carbonate. Rather, each carbonate mineral tends to display specific carbon  
303 isotope composition: siderite crystals range between  $\delta^{13}\text{C} = -5.12\text{‰}$  and  $-4.15\text{‰}$ , ankerite crystals  
304 range between  $-3.6\text{‰}$  and  $-5.1\text{‰}$ , whereas apart from one sample ( $\delta^{13}\text{C} = -2.5\text{‰}$ ), calcite crystals are  
305 more depleted in  $^{13}\text{C}$  and range between  $-11.2\text{‰}$  and  $-5.7\text{‰}$ . With the exception of two calcite  
306 crystals ( $\delta^{18}\text{O} = 11.9\text{‰}$  and  $\delta^{18}\text{O} = 16.1\text{‰}$ ), carbonate grains display similar and homogeneous  $\delta^{18}\text{O}$   
307 values, in the 19-25 ‰ range.

308 Figure 9 indicates that gangue carbonates plot in the range of hydrothermal carbonates. Calculation of  
309 the isotopic composition of the hydrothermal fluid in equilibrium with gangue carbonates is required  
310 in order to determine the origin of the hydrothermal fluid. Based on fluid inclusion analysis performed  
311 on galena from Signal vein, Nerci (2006) and Marcoux et al. (2015) estimated a minimum trapping  
312 temperature of about 230°C for the Pb-Zn-Ag veins. The oxygen isotope composition of the fluid in  
313 equilibrium with gangue carbonates was calculated for the range 230°C-300°C using the temperature-  
314 dependent calcite-H<sub>2</sub>O fractionation factors of Zheng (1999). The carbon isotope composition of CO<sub>2</sub>  
315 was calculated for the same temperature range using the temperature-dependant calcite-CO<sub>2</sub>  
316 fractionation factors of Chacko et al. (1991), assuming a similar fractionation for siderite and ankerite.  
317 The  $\delta^{18}\text{O}$  values of the hydrothermal fluid are consistent with those of a fluid in equilibrium with the  
318 surrounding shales (Tartèse et al., 2012; Figure 9). The calculated  $\delta^{18}\text{O}$  compositions of fluids in  
319 equilibrium with calcite crystals show significant variability. Indeed, two calcite samples display low  
320 oxygen isotope compositions, which likely reflect crystallization at higher temperature, from a low-  
321  $\delta^{18}\text{O}$  fluid component and/or variable fluid-rock ratios. The carbon isotope compositions of the  
322 hydrothermal fluid cover a wide range, between  $-9.6\text{‰}$  and  $-2.1\text{‰}$ . As calcite-CO<sub>2</sub> carbon  
323 fractionation is rather limited at 230-300°C, this large interval is unlikely the result of crystallization at  
324 variable temperature. It most likely reflects mixing between two end-members. The enriched  $^{13}\text{C}$  end-  
325 member could either be attributed to seawater-derived fluid or to a fluid that underwent interaction  
326 with ancient marine carbonates. The occurrence of carbonate-rich crustal rocks in Devonian and  
327 Viséan metasediments (sandy limestone and limestones + calcschists respectively) of the TJAD, and  
328 their possible occurrence in some underlying Cambrian and Proterozoic rocks (Gasquet et al., 2008;  
329 Pereira et al., 2015; and references therein) is consistent with the latter hypothesis. The depleted  $^{13}\text{C}$   
330 end-member has  $\delta^{13}\text{C}$  values typical of fluids with some organic carbon, regardless of their origin. It

331 would be hazardous to specify the exact source of fluid on the basis of the  $\delta^{13}\text{C}$  signature considering  
 332 that (i) Pb-Zn-Ag mineralization is coeval with magmatic activity, (ii) the surrounding Paleozoic  
 333 metasediments contain some organic matter, especially the Siluro-ordovician black shales and schists,  
 334 and (iii) the  $^{40}\text{Ar}/^{36}\text{Ar}$  ratios of sulphide crystals provide evidence of the infiltration of meteoric fluids.  
 335 Therefore, the carbon and oxygen compositions suggest that gangue carbonates precipitated from a  
 336  $\text{H}_2\text{O}-\text{CO}_2$ -rich fluid, with a strong crustal component, that equilibrated with the Paleozoic  
 337 metasedimentary pile hosting the Pb-Zn-Ag mineralization.

338

#### 339 4.3. $\epsilon_{\text{Nd}}$ results

340 Calcite and ankerite samples have rather similar Sm/Nd ratios and Nd isotopic compositions to those  
 341 of siderites from Castorina and Masi (2008; Table 3), with  $^{147}\text{Sm}/^{144}\text{Nd} = 0.1381$  to  $0.2532$  and  $\epsilon_{\text{Nd}} = -$   
 342  $4.84$  to  $-9.01$ .  $\epsilon_{\text{Nd}}$  values were calculated at the age of Pb-Zn-Ag ore formation (about 255 Ma; Rossi et  
 343 al., 2016). Results are presented in Table 3 and Figure 10. All carbonates display  $\epsilon_{\text{Nd}-255\text{Ma}}$  values of  $-4$   
 344 to  $-8$ . This range lies between the Paleozoic schists and the late-Carboniferous granitic stocks values  
 345 (Schaltegger et al., 1994; Castorina and Masi, 2008; Marcoux et al., 2015), suggesting Nd could derive  
 346 from these two crustal reservoirs. Permian rocks overlying the paleozoic schists at the time of the Pb-  
 347 Zn-Ag hydrothermal event, and deeper crustal rocks could also be taken into consideration. As these  
 348 rocks are not cropping out in the Central Meseta, there is no geochemical data available, so that their  
 349 contribution is not being discussed below. The contribution of the two assumed local crustal reservoirs  
 350 seems to be variable considering that some siderites have  $\epsilon_{\text{Nd}}$  values similar to those of some granitic  
 351 stocks from the district, whereas calcites display values close to those of Paleozoic basement rocks.  
 352 Castorina and Masi (2008) estimated a contribution of about 50 % for each reservoir, but they  
 353 considered leaching to have occurred at 280 Ma. Considering that Pb-Zn-Ag ore formed at 255 Ma  
 354 (Rossi et al., 2016) the basement contribution was estimated for each sample, using the equation below  
 355 with average  $\epsilon_{\text{Nd}-255\text{Ma}}$  values of  $-2.32$  for the granitic stocks and of  $-10.21$  for basement schists  
 356 (Castorina and Masi, 2008; see Table 3):

$$357 \quad \% \text{ basement} = (\epsilon_{\text{Nd sample}} - \epsilon_{\text{Nd granite}}) / (\epsilon_{\text{Nd sample}} - \epsilon_{\text{Nd granite}})$$

358 Nd from Paleozoic schists would thus contribute 58-71 % in calcite, 44-64 % in ankerite, and 22 to  
 359 59 % in siderite (using data from this study and from Castorina and Masi, 2008).

360

#### 361 4.4. Rare gases Ar-He

362 The W-Au and Pb-Zn-Ag mineralizations have rather similar  $^{40}\text{Ar}/^{36}\text{Ar}$  ratios, ranging between 284  
 363 and 328 (Figure 11), with the exception of one data point. Such values are similar to meteoric Ar  
 364 ( $^{40}\text{Ar}/^{36}\text{Ar} = 295.5$ ; Steiger and Jäger, 1977), providing evidence of infiltration of a meteoric and/or  
 365 air-equilibrated fluid for both mineralization. On the contrary, two distinct signatures are evidenced  
 366 from He isotopes (Figure 11): (i) the W-Au mineralization displays rather high air-normalized  $^3\text{He}/^4\text{He}$

367 ratios, ranging from 1.083 to 1.814, whereas (ii) the Pb-Zn-Ag mineralization displays very low air-  
 368 normalized  $^3\text{He}/^4\text{He}$  ratios, in the range 0.018-0.103.

369 Possible artifacts such as cosmogenic production of  $^3\text{He}$ , nucleogenic production of  $^3\text{He}$  from reaction  
 370 with a Li-rich crustal fluid, and isotopic fractionation during He-leakage have been discarded to  
 371 explain the measured  $^3\text{He}/^4\text{He}$  ratios because: all samples were collected several hundred meter below  
 372 the surface or from drillcores, so they cannot be affected by cosmogenic radiation; Li does not  
 373 substitute for Pb in galena (Kendrick et al., 2005) and fluid inclusion studies provided no evidence of  
 374 interaction with a Li-rich fluid (Marcoux et al., 2015); and if fractionation occurred during leakage,  
 375 preferential escape of  $^3\text{He}$  over  $^4\text{He}$  from galena would have produced  $^3\text{He}/^4\text{He}$  ratios lower than  
 376 crustal values, which has not been observed (Kendrick et al., 2005; Bouabdellah et al., 2015). The  
 377 measured  $^3\text{He}/^4\text{He}$  ratios are thus assumed to reflect mixing between atmospheric, crustal and mantle-  
 378 derived He ( $^3\text{He}/^4\text{He}_{\text{atmt}} = R_a = 1.39 \times 10^{-6}$ ;  $^3\text{He}/^4\text{He}_{\text{crust}} = 0.01\text{-}0.05 R_a$ ;  $^3\text{He}/^4\text{He}_{\text{mantle}} = 6\text{-}9 R_a$ ; Andrews,  
 379 1985; Porcelli et al., 1992, Burnard et al., 1999; Burnard and Poly, 2004).

380 Even though a sample has a  $^3\text{He}/^4\text{He}$  ratio similar to atmospheric He, a contribution of atmospheric He  
 381 is rather unlikely for the W-Au ores. Considering a  $^3\text{He}/^4\text{He}_{\text{mantle}}$  ratio of  $6 R_a$ , more than 95 % of He  
 382 from the W-Au ores would derive from atmospheric He, which is very unlikely considering that the  
 383 W-Au mineralization is genetically related to late-Variscan calc-alkaline magmatic activity (Cheilletz,  
 384 1984; Cheilletz and Isnard, 1985; Marcoux et al., 2015). Assuming atmospheric He contribution is  
 385 negligible for the W-Au mineralization, and considering a  $^3\text{He}/^4\text{He}_{\text{crust}}$  ratio of  $0.01 R_a$ , 18 % to 30 % of  
 386 the  $^4\text{He}$  derived from the mantle and 70% to 82% derived from the crust.

387 Sulphides from the Pb-Zn-Ag mineralization have air-normalized  $^3\text{He}/^4\text{He}$  ratios in the same range as  
 388 crustal He.  $^4\text{He}$  thus essentially has a crustal component and only exhibits very limited mixing with  
 389 atmospheric He (< 5 %) or mantle-derived He (< 2%).

390

#### 391 4.5. Lead isotopes

392 Lead isotope ratios from the Pb-Zn-Ag (galena) and the W-Au (mispickel and löllingite) ores as well  
 393 as data from the outcropping granitic stocks (K-feldspar) are presented in Figure 12 and Table 5  
 394 (Watanabe, 2001; Nerci, 2006; Marcoux et al., 2015; Tarrieu, 2015; Cheilletz et al., 2015). The lead  
 395 isotope signatures of sphalerite crystals show huge dispersion so that it is impossible to interpret the  
 396 data; they are thus not taken into consideration. Lead isotope data of galena samples spread between a  
 397 highly radiogenic end-member ( $^{207}\text{Pb}/^{204}\text{Pb} = 15.70$  to  $15.80$ ) and a much less radiogenic one  
 398 ( $^{207}\text{Pb}/^{204}\text{Pb} = 15.40$ ), thus suggesting mixing of distinct sources of lead. The dataset is bordered by  
 399 two mixing lines corresponding to the *ca.* 320 Ma and the *ca.* 255 Ma geochrons (trends A and B  
 400 respectively in Figure 12) that crosscut the crustal evolution curves of Stacey and Kramers (1975) and  
 401 Ludwig et al. (1989). Galena samples following trend A plot between lead isotope ratios observed in  
 402 K-feldspars from the outcropping stocks ( $^{207}\text{Pb}/^{204}\text{Pb} = 15.70$  and  $^{206}\text{Pb}/^{204}\text{Pb} = 18.30$ ) and a less  
 403 radiogenic composition ( $^{207}\text{Pb}/^{204}\text{Pb} = 15.55$  and  $^{206}\text{Pb}/^{204}\text{Pb} = 18.15$ ). Galena samples following trend

404 B plot between highly radiogenic ( $^{207}\text{Pb}/^{204}\text{Pb} = 15.80$  and  $^{206}\text{Pb}/^{204}\text{Pb} = 18.50$ ) and much less  
405 radiogenic values ( $^{207}\text{Pb}/^{204}\text{Pb} = 15.40$  and  $^{206}\text{Pb}/^{204}\text{Pb} = 18.05$ ). Trends A and B are not associated  
406 with specific veins or samples. Indeed, galena samples from Signal vein (blue symbols), as well as  
407 from Sidi Ahmed (green symbols), plot on both trends. Furthermore, some galena crystals from  
408 sample Tz10/42 (Signal vein) plot along trend A, some along trend B, and the others plot between the  
409 two trends, suggesting remobilisation of lead from different sources.

410 The least radiogenic ratios observed in the  $^{207}\text{Pb}/^{204}\text{Pb}$  versus  $^{206}\text{Pb}/^{204}\text{Pb}$  diagram suggest a deep  
411 source of lead such as the mantle or lower crust (e.g., Zartman and Haines, 1988; Figure 12). In  
412 contrast, the most radiogenic ratios clearly indicate leaching of lead from the upper crust. A possible  
413 source of radiogenic lead could thus be the outcropping granitic stocks. U-Pb dating of zircons from  
414 the magmatic stock indicates a crystallisation age of 320-300 Ma, whereas dating of monazite hosted  
415 in gangue carbonate yields an age of  $254 \pm 16$  Ma for the Pb-Zn-Ag ore (Rossi et al., 2016). As  
416 leaching of magmatic lead occurred several million years after the stocks crystallization, radiogenic  
417 ingrowth of Pb in U-rich magmatic crystals must be considered in order to determine the isotopic  
418 composition of the granitic stocks at the time of galena formation. Considering K-feldspar recorded  
419 the magmatic isotopic composition at the time of crystallization (ca. 320 Ma), the lead isotope  
420 signature of the granitic stocks at 255 Ma can be estimated at  $^{207}\text{Pb}/^{204}\text{Pb} = 15.70$  and  
421  $^{206}\text{Pb}/^{204}\text{Pb} = 18.40$ , using a  $^{238}\text{U}/^{204}\text{Pb}$  ratio of 9.735 (e.g., Faure and Mensing, 2005). Such ratios fit  
422 well with trend B (Figure 12), suggesting leaching at 255 Ma of lead from U-rich magmatic minerals  
423 formed at 320-310 Ma in the granitic stocks. As these stocks are rich in magmatic sulphides that  
424 contain traces of Pb but almost no U or Th, such as pyrite, sphalerite and chalcopryrite (Cheilletz,  
425 1984; Tarrieu, 2014), the most radiogenic ratios observed along trend A likely result from  
426 remobilisation of lead from these magmatic sulphides at 255 Ma. Concerning trend B, the most  
427 radiogenic Pb ratios ( $^{207}\text{Pb}/^{204}\text{Pb} = 15.80$ ) likely, result from leaching of highly radiogenic upper  
428 crustal rocks. As the upper crust is mainly composed of Paleozoic formations (black schists and  
429 limestones) and Permian sediments at the time of the Pb-Zn-Ag ore precipitation, these rocks likely  
430 provide the high radiogenic lead isotope signature. Even though, more data would be required in  
431 order to confirm this hypothesis, Pb inheritance from the country rocks has been evidenced in many  
432 Pb deposits (e.g., Marcoux and Moëlo, 1991).

433 Pb isotope data thus indicate a complex system, involving a deep source of lead (mantle and/or lower  
434 crust) and remobilisation of Variscan lead at 255 Ma (trend A), together with mobilisation of more  
435 radiogenic crustal lead at 255 Ma (trend B).

436

## 437 **5. Discussion**

### 438 *5.1. Metal and fluid sources*

439 Datasets obtained by combining various analytical methods indicate no crystallographic, paragenetic  
440 or vein control, suggesting that the Pb-Zn-Ag mineralization of the polymetallic Tighza district

441 crystallized from a single hydrothermal event, with the four paragenetic sequences highlighting the  
442 reactive fluid evolution in time.

443 The geochemical data clearly indicate that the W-Au and the Pb-Zn-Ag ores precipitated from  
444 different fluid sources. The hydrothermal fluid related to the W-Au ores derived from coeval  
445 magmatism (e.g., Cheilletz and Zimmerman, 1982; Giuliani et al., 1987; Marcoux et al., 2015), with a  
446 contribution of 20 to 30 %, of mantle-derived fluids evidenced in this study from He isotopes, as well  
447 as mixing with some meteoric fluids (Ar isotopes; Figure 13B). On the contrary, all geochemical data  
448 from this study and from the literature converge and indicate that the Pb-Zn-Ag mineralization is  
449 associated with a complex hydrothermal system involving various lead and fluid reservoirs (Figure  
450 13C), with (i) an important crustal component evidenced by REE in gangue carbonates as well as He,  
451 O, C, Nd and Pb isotopes, (ii) a meteoric component evidenced by Ar isotopes, and (iii) a deep source  
452 (mantle or lower crust) evidenced by Pb isotopes. As shown from O-C, Nd and Pb isotopes, the crustal  
453 component likely reflects at least two crustal reservoirs with varying contributions: the late-  
454 Carboniferous granitic stocks and the Paleozoic metasediments. Even though the involvement of the  
455 two crustal reservoirs and the meteoric source have already been proposed by Castorina and Masi  
456 (2000, 2008) using Sr and Nd analyses on siderites from Signal and Sidi Ahmed veins, this study  
457 confirms and strengthens the hydrothermal model and presents the first evidence for the implication of  
458 a deeper source (mantle and/or lower crust). Permo-triassic dikes have high-K calc-alkaline signature  
459 that reflects either an enriched mantle or a lower crustal component (Gasquet and Bouloton, 1995;  
460 Youbi et al., 1996), which is consistent with this deep reservoir being the source of Permo-triassic  
461 magmatism. However, as He data show no evidence of any significant mantle contribution for the Pb-  
462 Zn-Ag mineralization, the deeper source evidenced from relatively unradiogenic Pb ratios in Figure 12  
463 most likely represent a contribution of lower crustal rocks. Therefore, the hydrothermal fluid  
464 associated with the Pb-Zn-Ag deposit has a strong crustal component and results from mixing of  
465 crustal fluids, magmatic fluids (likely derived from lower crust anatexis, see below) and meteoric  
466 fluids. The resulting complex reactive fluid is compatible with fluid inclusion data from Nerci (2006)  
467 and Marcoux et al. (2015) who evidenced Na-Ca brines as well as a complex fluid implying organic  
468 compounds. A more detailed study would be required in order to determine the importance of the  
469 Permo-triassic magmatic fluids relative to the other crustal fluids.

470 The occurrence of late P4-calcite (group 2) with distinct REE+Y patterns than gangue carbonates of  
471 group 1 and the presence of synchysite as the main REE-bearing phase in gangue carbonates provide  
472 evidence of a later hydrothermal alteration of primary monazite and xenotime from H<sub>2</sub>O-CO<sub>2</sub>-F-rich  
473 fluids (Förster, 2001).

474

## 475 5.2. Genetic consideration and geodynamic implications

476 Rossi et al (2016) demonstrated that at least three successive magmatic-hydrothermal events occurred  
477 in the TJAD between late-Carboniferous and middle-Triassic (Figure 13):

478 1- Late-Carboniferous magmatic activity produced first the outcropping granitic stocks (320-300 Ma,  
479 Figure 13A; Tarrieu, 2014; Cheillett et al., 2015; Rossi et al., 2016).

480 2- The W-Au deposit results from a magmatic-hydrothermal event at 295-280 Ma (Cheillett and  
481 Zimmerman, 1982; Watanabe 2002; Cheillett et al., 2015; Marcoux et al., 2015; Rossi et al., 2016)  
482 that is related to the intrusion of a thin and shallow hidden pluton (Figure 13B; El Dursi, 2009). The  
483 related hydrothermal fluid has a strong magmatic origin (Marcoux et al., 2015), with a significant  
484 mantellic component, which is consistent with the late-Carboniferous high-K calc-alkaline magmatism  
485 having a deep source (Gasquet et al., 1996; El Hadi et al., 2006). This hydrothermal fluid was mixed  
486 with meteoric fluids (Figure 13B). The late-Carboniferous and Permian extensional tectonics induced  
487 a crustal thinning (Michard et al., 2008; and references therein) and melting of the underlying mantle  
488 and lower crust to produce calc-alkaline magmas (Gasquet et al., 1996; El Hadi et al., 2006). Magma  
489 emplacement generated high-temperature hydrothermal fluids that mobilized metals from the  
490 surrounding rocks (Marcoux et al., 2015), produced a hydrothermal alteration halo (Cheillett, 1984;  
491 Cheillett and Isnard, 1985) and lead to W-Au precipitation at high temperature. As proposed by  
492 Marcoux et al. (2015), the W-Au mineralization can thus be considered as an intrusion-related gold  
493 deposit. In addition, due to the occurrence of large dissemination patterns, W-rich skarn, stockwerks,  
494 sheated veins and large W-Au veins, this deposit can also be considered as a porphyry-type deposit, in  
495 an extensional context (e.g., Seedorff et al., 2005).

496 3- Dating of the Pb-Zn-Ag mineralization at  $254 \pm 16$  Ma indicate that this hydrothermal event is  
497 clearly disconnected with, but superimposed to the W-Au mineralization between late-Permian and  
498 Middle Triassic (Tarrieu, 2014; Cheillett, et al., 2015; Rossi et al. 2016). During that period, the  
499 extensional tectonic regime and crustal thinning intensifies, and magmatic activity evolves from  
500 plutonic to hypovolcanic in the TJAD (Agard et al., 1958; Cheillett, 1984; Youbi et al., 1995; Tarrieu,  
501 2014; Rossi et al., 2016). Reactivation of the old dextral crustal-scale shear zones in a sinistral tectonic  
502 regime leads to opening of SW-NE tension-gashes that channel magmas and hydrothermal fluids  
503 (Figure 2). The emplacement of a dense network of high-K calc-alkaline to alkaline dikes increases the  
504 regional heat flux, which triggers circulation of hydrothermal crustal fluids. During fluid flow, these  
505 fluids leached the upper crustal rocks, including the Paleozoic metasediments, late-Carboniferous  
506 granites and possibly the Permian detrital sediments (Figure 13C). Mixing with meteoric fluids  
507 occurred, as well as various degrees of mixing with Permo-triassic magmatic fluids. The Pb-Zn-Ag  
508 mineralization can be considered an epithermal vein-type as it developed in association to high-K calc-  
509 alkaline to alkaline volcanic activity (Youbi et al., 1995; Tarrieu, 2014; Rossi et al., 2016), under  
510 rather low temperatures ( $T > 230^{\circ}\text{C}$ ; Nerci, 2006; Marcoux et al., 2015), at shallow crustal levels  
511 (Youbi et al., 1995), and mostly involved hydrothermal crustal fluids.

512 The occurrence of a later hydrothermal event is evidenced in the TJAD by a change in REE+Y pattern  
513 of late calcite, and by the alteration of primary monazite and xenotime into synchysite. This reaction  
514 involves circulation of late H<sub>2</sub>O-CO<sub>2</sub>-F-rich fluids. Similar fluids have been described in the



515 neighboring El Hammam deposit (dated at  $205 \pm 1$  Ma by Cheilietz et al., 2010; Zemri et al., 2015),  
516 the Zrahina deposit, which is assumed to be Permo-triassic in age from field observations (Jébrak,  
517 1982), and the El Aouli deposit (Margoume et al., 2015). The hydrothermal activity that developed  
518 during Triassic-Jurassic extensional tectonic regime thus likely affected the Tighza district.

519 Sb-Ba mineralization is also present in the TJAD, though its age is poorly constrained. Its  
520 geochronological and genetic position relative to the two other mineralization events is not known  
521 with certainty but is probably younger (Agard et al., 1958).

522 Radiometric ages of magmatic-hydrothermal activity from Tarrieu (2014) and Rossi et al. (2016)  
523 constrain the timing of the model proposed by Marcoux et al. (2015) for the TJAD: the Pb-Zn-Ag  
524 mineralization appears to be clearly disconnected from the W-Au mineralization, as it is about 30 Ma  
525 younger. Therefore, the model proposed in this paper diverges from Marcoux et al. (2015). For these  
526 authors, the Pb-Zn-Ag mineralization is related to fluid focusing at the top of the solidified and cold  
527 intrusion that produced the W-Au mineralization. In our model, the Pb-Zn-Ag mineralization is  
528 triggered by Permo-triassic magmatic activity due to post-Variscan extensional tectonics. The ore  
529 deposits of the TJAD are thus spatially associated with multiple intrusions of Cordilleran-type calc-  
530 alkaline magmatism (cf., Sillitoe 2010; Catchpole 2011). Fluid flow and related polymetallic  
531 mineralization were generated during a late-Variscan to Permo-Triassic transpressional regime  
532 (Michard et al., 2008) that favoured the development of mantle and crust-derived magmas. These two  
533 events belong to a key period between the end of the Variscan belt formation in Morocco and the  
534 beginning of the Atlantic Ocean opening in the region as highlighted by Liassic volcanism of the  
535 CAMP (Mahmoudi and Bertrand, 2007; Verati et al., 2007, Margoume et al., 2015).

536 The occurrence of hydrothermal and magmatic activity during Permian and Triassic times was not  
537 limited to the Moroccan Meseta. The Aouli Pb-Zn veins from the Upper Moulouya district (Eastern  
538 Mesesta, Morocco) formed in a similar context to the Tighza Pb-Zn-Ag ore. According to Jébrak et al.,  
539 (1998) and Margoume et al., (2015), lead was leached from neighbouring Variscan granites and from  
540 underlying Proterozoic rocks between 250 and 210 Ma. The Aouli deposit thus seems to be nearly  
541 contemporaneous with the Tighza Pb-Zn-Ag event. In the Central Pyrenees, several Pb-Zn-Ag vein-  
542 type deposits are associated with Permo-Triassic hydrothermal activity that resulted in lead leaching  
543 from the surrounding bedrock and remobilization from previously formed Pb-rich ore deposits (e.g.,  
544 Munoz et al., 2015; Subías et al., 2015; and references therein). As shown from Pb isotopic signatures  
545 of the Pb-Zn-Ag mineralization, similar remobilization of older Pb occurred in the TJAD. Permo-  
546 Triassic Pb-Zn-Ag vein-type ores hosted in Variscan basement thus likely result from crustal thinning  
547 and resulting melting that preceded the Atlantic Ocean rifting. The occurrence of a deep source of lead  
548 has only been observed in the TJAD, probably because of its more westward location (Murphy et al.,  
549 2016). Indeed, at 250-230 Ma, the continental crust was the most thinned in the vicinity of the future  
550 rift axis, so that melting affected deeper crustal levels (e.g., Tighza district) than further East (e.g.,  
551 upper Moulouya in Central Morocco and Pyrenean deposits).

552 The model proposed for the TJAD is actually consistent with other Pb-Zn-Ag(-F) deposits of similar  
553 age or geological context (extensional and transcurrent tectonic regime, reactivation of crustal-scale  
554 faults and shear zones, etc.) that are hosted in Palaeozoic basement rocks such as Freiberg (Germany),  
555 Harz (Germany) and Coeur d'Alene (Idaho). As for the TJAD, the genesis of these deposits also  
556 involves fluid mixing of a deep-seated hydrothermal fluid, with crustal fluids and meteoric fluids  
557 under low temperatures (250-300°C), in disconnection with the local plutonic rocks (e.g., Beaudoin  
558 and Sangster, 1992; Paiement et al., 2012).

559

560

## 561 **6. Concluding remarks**

562 The combination of several isotopic methods provided key data to unravel the complexity of the  
563 hydrothermal system associated with the Pb-Zn-Ag mineralization of the TJAD. The multi-proxy  
564 approach better constrains the various lead and fluid sources for the Pb-Zn-Ag mineralization. Rare  
565 earth elements (REE) content of gangue carbonates, and C-O, Sm-Nd, Ar-He and Pb-Pb isotopic data  
566 indicate that the Pb-Zn-Ag mineralization likely resulted from mixing of (i) hydrothermal crustal  
567 fluids that interacted with the surrounding late-Carboniferous granites and Paleozoic metasediments,  
568 (ii) Permo-triassic magmatic fluids resulting from the melting of lower crustal rocks, and (iii)  
569 meteoritic fluids,. The hydrothermal activity and the associated base metal deposits were triggered by  
570 Permo-Triassic magmatism produced by the extensional tectonics that pre-dates the Atlantic Ocean  
571 opening, which is evidenced by a dense SW-NE-trending magmatic dike network. Therefore, the late-  
572 Variscan intrusion-related model must definitively be abandoned to explain the Pb-Zn-Ag ore  
573 formation. The polymetallic Tighza-Jbel Aouam district results from the occurrence of a hydrothermal  
574 activity related to several magmatic episodes and geodynamic events during late Carboniferous to  
575 early Triassic times (Rossi et al., 2016; this study): (1) sterile late-carboniferous felsic intrusion, (2) a  
576 reduced intrusion-related W-Au mineralization in early Permian, (3) a Pb-Zn-Ag mineralization  
577 triggered by Permo-Triassic magmatic activity in an extensional tectonic regime, (4) later circulation  
578 of a H<sub>2</sub>O-CO<sub>2</sub>-F-rich, possibly late-Triassic in age.

579 The metallogenic model proposed for the Pb-Zn-Ag Tighza-Jbel Aouam deposit provides new  
580 constraints for Pb-Zn-Ag exploration strategies in the Moroccan Meseta. Exploration targets must take  
581 into account the following discriminant geological features: (i) Permo-triassic high-K calc-alkaline to  
582 alkaline dikes, (ii) extensional tectonics and reactivation of ancient crust-scale faults or shear zones,  
583 (iii) Paleozoic metasediments containing organic matter (e.g., black shales) subjected to low grade  
584 metamorphism (e.g., greenschist facies).

585

## 586 **Acknowledgments**

587 This study was supported by INSU-CNRS through the CESSUR program, by a collaboration  
588 agreement between Université Savoie Mont Blanc and the Compagnie Minière de Touissit (CMT). It

589 was part of Leïla Tarrieu's PhD at the University of Savoie-Mont-Blanc, supported by the French  
590 Ministry for Research and Higher Education. This paper is dedicated to the memory of Pete Burnard,  
591 who passed away in 2015, and who provided the Ar-He data and thus contributed to better  
592 understanding the fluid sources of the polymetallic district of Tighza-Jbel Aouam. The authors are  
593 thankful to Mohammed Bouabdellah for his constructive remarks that help improving this manuscript,  
594 and to an anonymous reviewer.

595

## 596 **References**

- 597 Agard, J., Balcon, J.M., Morin P., 1958. Etude géologique de la région minéralisée du Jebel Aouam  
598 (Maroc central). Notes Mémoires Service Géologique Maroc 132, 127.
- 599 Andrews, J.N., 1985. The isotopic composition of radiogenic helium and its use to study groundwater  
600 movement in confined aquifers. *Chemical Geology* 49, 339-351.
- 601 Arribas, A.Jr., Tosdal, R.M., 1994. Isotopic composition of Pb in ore deposits of the Betic Cordillera,  
602 Spain: origin and relationship to other European deposits. *Economic Geology* 89, 1074-1093.
- 603 Bamoumen, H., Aarab, M. Soulimani, A., 2008. Evolution tectono-sédimentaire et magmatique des  
604 bassins viséen supérieur d'Azrou-Khenifra et des Jebilet orientales (Meseta marocaine). *Estudio*  
605 *Geologicos* 64 (2), doi:10.3989/egeol.08642.020.
- 606 Bau, M., 1991. Rare-earth element mobility during hydrothermal and metamorphic fluid-rock  
607 interaction and the significance of the oxidation state of europium. *Chemical Geology* 93, 219-230.
- 608 Bau, M., Möller, P., 1992. Rare earth element fractionation in metamorphogenic hydrothermal calcite,  
609 magnesite and siderite. *Mineralogy and Petrology* 45, 231-246.
- 610 Beaudoin, G., Sangster, D.F., 1992. Descriptive model for Silver-Lead-Zinc Veins in Clastic  
611 Metasedimentary Terranes. *Economic Geology* 87, 1005-1021.
- 612 Bouabdelli, M., Piqué, A., 1996. Du bassin sur décrochement au bassin d'avant-pays: Dynamique du  
613 bassin d'Azrou-Khenifra (Maroc hercynien central). *Journal of African Earth Sciences* 23, 213-224.
- 614 Bouabdellah, M., Beaudoin, G., Leach, D.L., Grandia, F., Cardellach, E., 2009. Genesis of the Assif El  
615 Mal Zn-Pb (Cu-Ag) vein deposit. An extension-related Mesozoic vein system in the High Atlas of  
616 Morocco. Structural, mineralogical and geochemical evidence. *Mineralium Deposita* 44, 689-704.
- 617 Bouabdellah, M., Niedermann, S., Velasco, F., 2015. The Touissit-Bou Beker Mississippi Valley-  
618 Type District of Northeastern Morocco: Relationships to the Messinian Salinity Crisis, Late  
619 Neogene-Quaternary Alkaline Magmatism, and Buoyancy-Driven Fluid Convection. *Economic*  
620 *Geology* 110, 1455-1484.
- 621 Bouloton, J., Gasquet, D., 1995. Melting and undercooled crystallisation of felsic xenoliths from  
622 minor intrusions (Jebilet massif, Morocco). *Lithos* 35, 201-219.
- 623 Boushaba, A., Marignac, C., 2009. La nature des fluides hydrothermaux des tourmalinites du massif  
624 granitique permien du Ment (Maroc central) : couplage de la mineralogie des tourmalines et de  
625 l'étude des inclusions fluides. *Collection EDYTEM* 9, 33-48.

- 626 Boutaleb, M., 1988) Reconstitution de l'évolution tectono-métamorphique, magmatique et  
627 hydrothermale du district stannio-wolframifère de Walmès (Maroc central). Implications  
628 métallogéniques. PhD thesis, INPL, Nancy, 268 p.
- 629 Burnard, P.G., Hu, R., Turner, G., Br, X.W., 1999. Mantle, crustal and atmospheric noble gases in  
630 Ailaoshan Gold deposits, Yunnan Province, China. *Geochimica et Cosmochimica Acta* 63(10),  
631 1595-1604.
- 632 Burnard, P.G., Polya, D.A., 2004. Importance of mantle derived fluids during granite associated  
633 hydrothermal circulation: He and Ar isotopes of ore minerals from Panasqueira. *Geochimica and*  
634 *Cosmochimica Acta* 68(7), 1607-1615.
- 635 Campbell, A., Larson, P., 1998. Introduction to stable isotope applications in hydrothermal ore  
636 deposits. *Reviews in Economic Geology* 6, 173-193.
- 637 Castorina, F., Masi, 2000. Sr-isotopic composition of siderite for assessing the origin of mineralizing  
638 fluids: the case study from the Jebel Awam deposit (Central Morocco). *Ore Geology Reviews* 17,  
639 83-89.
- 640 Castorina, F., Masi, U., 2008. REE and Nd-isotope evidence for the origin of siderite from the Jebel  
641 Awam deposit (Central Morocco). *Ore Geology Reviews* 34, 337-342.
- 642 Catchpole, H.P., 2011. Porphyry-related polymetallic mineralisation in the Morococha district, central  
643 Peru: mineralisation styles, timing and fluid evolution. PhD thesis, Genève University, Switzerland,  
644 288p.
- 645 Chacko, T., Mayeda, T.K., Clayton, R.N., Goldsmith, J.R., 1991. Oxygen and carbon isotopic  
646 fractionation between CO<sub>2</sub> and calcite. *Geochimica et Cosmochimica Acta* 55, 2867-2882.
- 647 Cheilletz, A., 1984. Contribution à la géologie du district polymétallique (W-Mo-Cu-Pb-Zn-Ag) du  
648 Djebel Aouam (Maroc central): application à la prospection des gisements de tungstène. Doctorat  
649 d'Etat, Institut National Polytechnique de Lorraine, France, 273 p.
- 650 Cheilletz, A., Zimmermann, J.L., 1982. Datations par la méthode K-Ar du complexe intrusif et des  
651 minéralisations en tungstène du Jbel Aouam (Maroc central). *Comptes Rendus Académie Sciences*,  
652 Série II, 295, 255-258.
- 653 Cheilletz, A., Isnard, P., 1985. Contribution à la prospection des gisements hydrothermaux de  
654 tungstène sur l'exemple du district polymétallique W-Pb-Zn-Ag du Jbel Aouam (Maroc central).  
655 *Mineral Deposita* 20, 220-230
- 656 Cheilletz, A., Gasquet, D., Filali, F., Archibald, D.A., Nespolo, M., 2010. A Late Triassic <sup>40</sup>Ar/<sup>39</sup>Ar  
657 age for the El Hamman high-REE fluorite deposit (Morocco): mineralization related to the Central  
658 Atlantic Magmatic Province? *Mineral Deposita* 45, 323-329.
- 659 Cheilletz, A., Rossi, M., Tarrieu, L., Gasquet, D., Bounajma, H., Mantoy, T., Ouazzani, L.,  
660 Ouchtouban, L., Deloule, E., Burnard, P., Paquette, J.L., 2015. A cordilleran zoning model for the  
661 polymetallic W-Au-Pb-Zn-Ag Tighza-Jbel Aouam District (Central Morocco): contribution from

- 662 new He-Ar and U-Th-Pb data. Proceedings of the 13<sup>th</sup> SGA meeting, Nancy (France), vol. 4, 1579-  
663 1582.
- 664 Deloule, E., Allègre, C.J., Doe, B., 1986. Lead and sulfur isotope microstratigraphy in galena crystals  
665 from Mississippi-Valley type deposits. *Economic Geology* 81, 1307-1321.
- 666 Desteucq, C., 1974. Le système filonien du Jbel Aouam (Maroc central); essai d'interprétation  
667 structurale. PhD thesis, University Paul Sabatier, Toulouse, France, 93p.
- 668 El Dursi, K., 2009. Minéralisations et circulations péri-granitiques: modélisation numérique couplée  
669 2D/3D, applications au district minier de Tighza (Maroc central). PhD thesis, University Orléans,  
670 France, 218p.
- 671 El Hadi, H., Simancas, J.F., Tahiri, A., Gonzalez Lodeiro, F., Azor, A., Martinez Poyatos, D., 2006.  
672 Comparative review of the Variscan granitoids of Morocco and Iberia: proposal of a broad zonation.  
673 *Geodinamica Acta* 19(2),103-116.
- 674 Faure, G., Mensing, T.M., 2005. *Isotopes: principles and applications*. Third edition, Wiley (ed.), 897p.
- 675 Field, C., Fifarek, R., 1985. Light stable-isotope systematics in the epithermal environment. Review in  
676 *Economic Geology* 2, 99-128.
- 677 Fontes, J.C., Andrews, J.N., Walgenwitz, F., 1991. Evaluation de la production naturelle in situ  
678 d'argon-36 via le chlore-36; Implications géochimiques et géochronologiques: Evaluation of natural  
679 in situ production of argon-36 via chlorine-36; Geochemical and geochronological implications.  
680 *Comptes Rendus de l'Academie des Sciences, Serie IIA* 313, 649-654.
- 681 Förster, H.J., 2001. Synchysite-(Y) - synchysite-(Ce) solid solutions from Markersbach, Erzgebirge,  
682 REE and Th mobility during high-T alteration of highly fractionated aluminous A-type granites.  
683 *Mineralogy and Petrology* 72(4), 259-280.
- 684 Gasquet, D., Bouloton, J., 1995. Les filons de microdiorite des Jebilet centrales (Meseta marocaine):  
685 pré-rifting permien ? Rés. Réunion. extraord. Société géologique de France, Marrakech, Abstract book,  
686 55.
- 687 Gasquet, D., Stussi, J.M., Nachit, H., 1996. Les granitoïdes hercyniens du Maroc, dans le cadre de  
688 l'évolution géodynamique régionale. *Bulletin Société géologique de France* 167(4), 517-528.
- 689 Gasquet, D., Ennih, N., Liégeois, J.P., Soulaïmani, A., Michard, A., 2008. The Pan-African belt. In :  
690 Michard et al., *Continental Evolution: The geology of Morocco*. Lecture notes in Earth Sciences 116,  
691 Springer Verlag Ed, 33-64.
- 692 Giuliani, G., Cheilletz, A., Mechiche, M., 1987. Behaviour of REE during thermal metamorphism and  
693 hydrothermal infiltration associated with skarn and vein-type tungsten ore bodies in central Morocco.  
694 *Chemical Geology* 64, 279-294.
- 695 Giuliani, G., Cheilletz, A., Zimmermann, J.L., 1989. The emplacement, geochemistry and  
696 petrogenesis of two central Morocco Hercynian granites. Geotectonic implications. *Journal of*  
697 *African Earth Sciences* 9, 617-629.
- 698 Guilbert, J.M., Park, C.F.Jr., 1999. *The geology of ore deposits*. Freeman and Co. (ed.), 985p.

- 699 Hecht, L., Freiberger, R., Gilg, H.A., Grundmann, G., and Kostitsyn, Y.A., 1999, Rare earth element  
700 and isotope (C,O,Sr) characteristic of hydrothermal carbonates: Genetic implications for dolomite-  
701 hosted talc mineralization at Göpfersgrün (Fichtelgebirge, Germany). *Chemical Geology* 155, 115-  
702 130.
- 703 Jacobsen, S.B., Wasserburg, G.J., 1980. Sm–Nd isotopic evolution of chondrites. *Earth and Planetary*  
704 *Science Letters* 50, 139-155.
- 705 Jébrak, M., 1982. Les districts à fluorine du Maroc Central. *Bulletin du BRGM II*, 211-221.
- 706 Jébrak, M., 1984. Contribution à l'histoire naturelle des filons (F-Ba) du domaine Varisque français et  
707 marocain. Essai de caractérisation structurale et géochimique des filons en extension et en  
708 décrochement dans les massifs centraux français et marocains. Doctorat d'Etat, University of  
709 Orléans, France, 467p.
- 710 Jébrak, M., 1985. Le district filonien à Pb-Zn-Ag et carbonates du Jebel Aouam (Maroc Central).  
711 *Bulletin de Minéralogie* 108, 487-498.
- 712 Jébrak, M., Marcoux, E., Nasloubi, M., Zaharaoui, M., 1998. From sandstone- to carbonate-hosted  
713 stratabound deposits: an isotope study of galena in the upper-Moulouya District (Morocco).  
714 *Mineralium Deposita* 33, 406-415.
- 715 Jones, A., Genge, M., Carmody, L., 2013. Carbonate melts and carbonatites. In: *Carbon in Earth*,  
716 Hazen, RM and Jones, AP and Baross, JA, (eds.) Ed. Mineralogical society of America, 280-322.
- 717 Kendrick, M.A., Burgess, R., Harrison, D., Bjorklykke, A., 2005. Noble gas and halogen evidence for  
718 the origin of Scandinavian sandstone-hosted Pb-Zn deposits. *Geochimica et Cosmochimica Acta* 69,  
719 109-129.
- 720 Kharaka, Y., Hanor, J., 2003. Deep Fluids in the Continents: I. Sedimentary Basins. *Treatise on*  
721 *Geochemistry* 5, 1-48.
- 722 Lüders, V., Möller, P., Dulski, P., 1993. REE fractionation in carbonates and fluorites. In: Möller, P.,  
723 and Lüders, V., eds., *Formation of hydrothermal vein deposits*: Berlin-Stuttgart, Gebrüder  
724 Bornträger, *Monograph Series on Mineral Deposits* 30, 133-150.
- 725 Ludwig, K.R., Vollmer, R., Turi, B., Simmons, K.R., Perna, G., 1989. Isotopic constraints on the  
726 genesis of base-metal ores in southern and central Sardinia. *European Journal of Mineralogy*, 1,  
727 657–666.
- 728 Mahmoudi, A., Bertrand, H., 2007. Identification géochimique de la province magmatique de  
729 l'Atlantique central en domaine plissé : exemple du Moyen Atlas marocain. *C. R. Geoscience* 339,  
730 545-552.
- 731 Marcoux, E., Moëlo, Y., 1991. Lead isotope geochemistry and paragenetic study of inheritance  
732 phenomena in metallogenesis: examples from base metal sulfide deposits in France. *Economic*  
733 *Geology* 86, 106-120.

- 734 Marcoux, E., Nerci, K., Branquet, Y., Ramboz C., Ruffet, G., Peucat, J.J., Stevenson, R., Jebrak, M.,  
735 2015. Late-Hercynian Intrusion-related gold deposits: an integrated model on the Tighza  
736 polymetallic district, central Morocco. *Journal of African Earth Science* 107, 65-88.
- 737 Margoum, D., Bouabdellah, M., Klügel, A., Banks, D.A., Castorina, F., Cuney, M., Jébrak, M.,  
738 Bozkaya, G., 2015. Pangea rifting and onward pre-Central Atlantic opening as the main ore-forming  
739 processes for the genesis of the Aouli REE-rich fluorite–barite vein system, Upper Moulouya  
740 District, Morocco. *Journal of African Earth Sciences* 108, 22-39.
- 741 Marignac, C., Cuney, M., 1999. Ore deposits in the French Massif Central: insight into the  
742 metallogensis of the Variscan collision belt. *Mineralium Deposita* 34, 472-504.
- 743 Marty, B., Zimmermann, L., 1999. Volatiles (He, C, N, Ar) in mid-ocean ridge basalts: assessment of  
744 shallow-level fractionation and characterization of source composition. *Geochimica et*  
745 *Cosmochimica Acta* 63(21), 3619-3633.
- 746 McLennan, S.M., 1989. Rare earth elements in sedimentary rocks: influence of provenance and  
747 sedimentary processes. *Reviews in Mineralogy* 21, 169-200.
- 748 Michard, A., 1989. Rare-earth element systematics in hydrothermal fluids. *Geochimica et*  
749 *Cosmochimica Acta* 53, 745-750.
- 750 Michard, A., Hoepffner, C., Soulaïmani, A., Baidder, L., 2008. The Variscan belt. In: Michard, A.,  
751 Saddiqi, O., Chalouan, A., Frizon de Lamotte, D. (eds) *Continental evolution: the geology of*  
752 *Morocco. Lecture Notes Earth Sci* 116, Springer-Verlag, Berlin-Heidelberg, 65-132.
- 753 Möller, P., Lüders, V., Schröder, J., Luck, J., 1991. Element partitioning in calcites as a function of  
754 solution flow rate: a study on vein calcites from the Harz Mountains. *Mineralium Deposita* 26, 175-  
755 179.
- 756 Munoz, M., Baron, S., Boucher, A., Béziat, D., Salvi, S., 2015. Mesozoic vein-type Pb–Zn  
757 mineralization in the Pyrenees: Lead isotopic and fluid inclusion evidence from the Les Argentie`  
758 res and Lacore deposits. *C.R. Géosciences, serie 2*, [http:// dx.doi.org/10.1016/j.crte.2015.07.001](http://dx.doi.org/10.1016/j.crte.2015.07.001).
- 759 Murphy, J.B., Quesada, C., Gutiérrez-Alonso, G., Johnston, S.J., Weil, A., 2016. Reconciling  
760 competing models for the tectonostratigraphic zonation of the Variscan orogen in western Europe,  
761 *Tectonophysics*, doi: 10.1016/j.tecto.2016.01.006.
- 762 Nerci, K., 2006. Les minéralisations aurifères du district polymétallique de Tighza (Maroc central): un  
763 exemple de mise en place périgranitique tardihercynienne. PhD thesis, Université d'Orléans –  
764 Université du Québec à Montréal, 302 p.
- 765 Paiement, J-Ph., Beaudoin, G., Paradis S. and Ullrich, T., 2012. Geochemistry and metallogeny of Ag-  
766 Pb-Zn veins in the Purcell Basin, British Columbia. *Economic Geology* 107, 1303–1320.
- 767 Pereira, M.F., El Houicha, M., Chichorro, M., Armstrong, R., Jouhari, A., El Attari, A., Ennih, N.,  
768 Silva, J.B., 2015. Evidence of a Paleoproterozoic basement in the Moroccan Variscan Belt  
769 (Rehamna Massif, Western Meseta). *Precambrian Research* 268, 61-73.

- 770 Pin, C., Zalduegui, J.F.S., 1997. Sequential separation of light rare-earth elements, thorium and  
771 uranium by miniaturized extraction chromatography: Application to isotopic analyses of silicate  
772 rocks. *Analytica Chimica Acta* 339, 79-89.
- 773 Piqué, A., Soulaïmani, A., Hoepffner, C., Bouabdelli, M., Laville, E., Amrhar, M., Chalouan, A., 2007.  
774 *Géologie du Maroc*, Ed. Géode, Marrakech, 287p.
- 775 Porcelli, D. R., O’Nions, R. K., Galer, S.G., Cohen, A.S., Matthey, D. P., 1992. Isotopic relationships  
776 of volatile and lithophile trace elements in continental ultramafic xenoliths. *Contribution Mineralogy  
777 and Petrology* 110, 528-538.
- 778 Rollinson, H., 1993. *Using geochemical data: Evaluation, presentation, interpretation*, 352p.
- 779 Rossi, M., and Tarrieu, L., Cheilletz, A., Gasquet, D., Deloule, E., Paquette, J.L., Bounajma, H.,  
780 Mantoy, T., Ouazzani, L., Ouchtouban, L., 2016 The polymetallic (W-Au/Pb-Zn-Ag) Tighza district  
781 (central Morocco): age of the magmatic and hydrothermal events. In: Bouabdellah, M., and Slack,  
782 J.F., eds., *Mineral deposits of North Africa*: Berlin-Heidelberg, Springer-Verlag. DOI: 10.1007/978-  
783 3-319-31733-5\_6.
- 784 Saadi, M., 1982. *Carte structurale du Maroc (1/2 000 000)*. Notes et mémoires du service géologique  
785 du Maroc.
- 786 Schaltegger, U., Stille, P., Rais, N., Piqué, A., Clauer, N., 1994. Neodymium and strontium isotopic  
787 dating of diagenesis and low-grade metamorphism of argillaceous sediments. *Geochimica et  
788 Cosmochimica Acta* 58, 1471-1481.
- 789 Sedorff, E., Dilles, J.H., Proffet, J.M., Enaudi, M.T., 2005. Porphyry deposits: characteristics and  
790 origins of hypogene features. In: *Economic Geology 100<sup>th</sup> Anniversary volume*, 251-298.
- 791 Sillitoe, R.H., 2010. Porphyry-copper systems. *Economic Geology* 105, 3-41.
- 792 Stacey, J.D., Kramers, J.D., 1975. Approximation of terrestrial lead isotope evolution by a two-stage  
793 model. *Earth Planetary Science Letters* 26, 207–221.
- 794 Steiger, R.H. and Jäger, E., 1977. Subcommittee on geochronology: Convention on the use of decay  
795 constants in geo- and cosmochronology. *Earth and Planetary Science Letters* 36(3), 359-362.
- 796 Subías, I., Fanlo, I., Billström, K., 2015. Ore-forming timing of polymetallic-fluorite low temperature  
797 veins from Central Pyrenees: a Pb, Nd and Sr isotope perspective. *Ore Geology Reviews* 70, 241-  
798 251.
- 799 Tarrieu, L., 2014. Nouvelles données minéralogiques, géochimiques et géochronologiques sur le  
800 gisement polymétallique de Tighza (Maroc Central) – Contribution à la métallogénie des gisements  
801 de métaux de base filoniens en contexte post-collisionnel. PhD thesis, University of Savoie, France,  
802 240p.
- 803 Tartèse, R., Boulvais, P., Poujol, M., Chevalier, T., Paquette, J-L., Ireland, T., Deloule, E., 2012.  
804 Mylonites of the South Armorican Shear Zone: Insight for crustal-scale fluid flow and water-rock  
805 interaction processes. *Journal of Geodynamics* 56, 86-107.



- 806 Torres-Ruiz, J., 2006. Geochemical constraints on the genesis of the Marquesado iron ore deposits,  
807 Betic Cardillera, Spain: REE, C, O and Sr isotope data. *Economic Geology* 101, 667-677.
- 808 Verati, C., Rapaille, C., Feraud, G., Marzoli, A., Bertrand, H., Youbi, N., 2007.  $^{40}\text{Ar}/^{39}\text{Ar}$  ages and  
809 duration of the Central Atlantic Magmatic Province volcanism in Morocco and Portugal and its  
810 relation to the Triassic-Jurassic boundary. *Palaeogeography, Palaeoclimatology, Palaeoecology* 244,  
811 308–325.
- 812 Wadjiny, A., 1998. Le plomb au Maroc: cas des districts de Touissit et de Jbel Aouam. *Chroniques*  
813 *de la Recherche Minière* 531-532, 9-28.
- 814 Watanabe, Y., 2001. Timing of volcano-sedimentary massive sulfide and vein-type Pb-Zn  
815 mineralization in the western meseta of Morocco:  $^{40}\text{Ar}-^{39}\text{Ar}$  geochronology. *Exploration Technology*  
816 *and interpreting methods Part IV, JICA-B.R.P.M project (1998-2002)*.
- 817 Watanabe, Y., 2002.  $^{40}\text{Ar}/^{39}\text{Ar}$  Geochronologic constraints on the timing of massive sulfide and vein-  
818 type Pb-Zn mineralization in the Western Meseta of Morocco. *Economic Geology* 97, 145-157.
- 819 Williams-Jones, A.E., Migdisov, A.A., Samson, I.M., 2012. Hydrothermal mobilization of the rare  
820 earth elements – a tale of “Ceria” and “Yttria”. *Elements* 8, 355-360.
- 821 Youbi, N., Cabanis, B., Chalot-Prat, F., Cailleux, Y., 1995. Histoire volcano-tectonique du massif  
822 permien de Khénifra (Sud-Est du Maroc Central). *Geodinamica Acta (Paris)* 8 (3), 158-172
- 823 Zartman, R.E., Haines, S.M., 1988. The plumbotectonic model for Pb-isotopic systematics among  
824 major terrestrial reservoirs – A case for bi-directional transport. *Geochimica et Cosmochimica Acta*  
825 52, 1327-1339,
- 826 Zemri, O., Bouabdellah, M., Jébrak, M., Sadequi, M., Gaouzi, A., Maacha, L., 2015. Geology and  
827 REE geochemistry of the El Hammam REE-rich fluorite deposit (Central Meseta, Morocco).  
828 *Proceedings of the 13<sup>th</sup> SGA meeting*, 1679-1682.
- 829 Zheng, Y.F., 1999. Oxygen isotope fractionation in carbonate and sulfate minerals, *Geochemical*  
830 *Journal* 33, 109-126.

831

832 **Figure captions**

833 **Figure 1.** A) Simplified geological map of central Morocco (modified from Youbi et al., 1995). B)  
834 Structural map of the Azrou-Khenifra basin in the Central Meseta (modified from Saadi, 1982;  
835 Bouabdelli and Piqué, 1996; Bamoumen et al., 2008).

836 **Figure 2.** Geological map of the polymetallic Tighza district in central Morocco. Modified from  
837 Agard et al. (1958), Cheilletz (1984), and CMT (pers. comm. 2013).

838 **Figure 3.** Relationships between Pb-Zn-Ag and W-Au mineralization: Pb-Zn-Ag veins cut W-Au  
839 veins in the roof of Structure 18.

840 **Figure 4.** A) Underground photograph showing banded mineralized vein from Filon Signal (sub-level  
841 13). B) Brecciated and banded Pb-Zn-Ag veins in Sidi Ahmed. P1, P2, P3 and P4 refer to the  
842 successive paragenetic sequences in Figure 5.

843 **Figure 5.** Paragenetic sequence of the Pb-Zn mineralisation. SA and IA stand for Sidi Ahmed and  
 844 Ighrem Aousser veins respectively.

845 **Figure 6.** REE total content of undifferentiated gangue carbonates from Tighza Pb-Zn-Ag veins. Data  
 846 from this study, Jébrak (1985) and Castorina and Masi (2008).

847 **Figure 7.** PAAS-normalized REE patterns of gangue carbonates from the main Pb-Zn-Ag veins of  
 848 Tighza district. Magmatic rock data from this study and from Giuliani et al., 1987). REE patterns of  
 849 carbonates from the El Hammam F-deposit are indicated for comparison (data from Cheilletz et al.,  
 850 2010; Zemri et al., 2015). PAAS normalization values from McLennan (1989).

851 **Figure 8.** REE-bearing phases hosted in gangue carbonates. A) and B) SEM pictures of synchysite  
 852 crystals hosted in gangue calcite. C) EDS spectra of synchysite. D) Ce-La-Y Ternary diagram showing  
 853 the composition of some synchysite crystals hosted in P4 calcite from Sidi Ahmed (Tz10/25) and  
 854 Ighrem Aousser (Tz10/32, Tz10/28).

855 **Figure 9.** Carbon and oxygen isotopic signatures of gangue carbonates from the Pb-Zn-Ag  
 856 mineralization (circles) and of a H<sub>2</sub>O-rich fluid in equilibrium with the carbonates at 230°C (squares;  
 857 see text for explanation). The isotopic ranges of terrestrial reservoirs are reported from Field and  
 858 Fifarek (1985), Rollinson (1993), Campbell and Larson (1998), Kharaka and Hanor (2003), Tartèse et  
 859 al., (2012) and Jones et al. (2013).

860 **Figure 10.**  $\epsilon_{Nd}$  of gangue carbonates, magmatic rocks and Paleozoic sediments at the time of Pb-Zn-  
 861 Ag ore formation (i.e., at 255 Ma; Rossi et al., 2016).  $\epsilon_{Nd-255Ma}$  values of local siderites have been  
 862 estimated using data from Castorina and Masi (2008),  $\epsilon_{Nd-255Ma}$  values of magmatic rocks have been  
 863 estimated using data from Castorina and Masi (2008) and Marcoux et al. (2015), and  $\epsilon_{Nd-255Ma}$  values  
 864 of Paleozoic rocks have been estimated using data from Castorina and Masi (2008; local rocks) and  
 865 Schaltegger et al. (1994; moroccoan Cambrian schists).  $\epsilon_{Nd-255Ma}$  of moroccoan Cambrian schists are in  
 866 the same range as Paleozoic schists from the Tighza district.

867 **Figure 11.**  $^{40}Ar/^{36}Ar$  and  $^3He/^4He$  (normalized to the atmospheric  $^3He/^4He$  ratio) of sulphide minerals  
 868 from W-Au (green) and Pb-Zn-Ag (red) deposits from Tighza district. Both deposits display meteoric  
 869 Ar signatures but distinct He signatures: while Pb-Zn-Ag ores have crustal He, the W-Au ores  
 870 evidence mixing with some mantle-derived He. Isotope ratios of the main geological reservoirs f from  
 871 Steiger and Jäger (1977), Andrews (1985), Fontes et al., (1991), Porcelli et al., (1992), Burnard et al.  
 872 (1999) and Burnard and Poly (2004).

873 **Figure 12.** Pb/Pb isotopic signatures of Pb-Zn-Ag veins, W-Au disseminations and granitoids from  
 874 this study, Watanabe (2001), Nerci (2006) and Marcoux et al. (2015). Note that the W-Au trend differs  
 875 from that of Pb-Zn-Ag.

876 **Figure 6.** Metallogenic model of the Tighza polymetallic district. The three main hydrothermal events  
 877 have been identified using U-Pb dating of zircon and Th-U dating of monazite (Rossi et al., 2016). A)  
 878 Crystallization of the outcropping granitic stocks at 320-300 Ma. B) Deposit of the W-Au ores in

879 relation with a hidden pluton at 300-280 Ma.. C) Deposit of the Pb-Zn-Ag ores in relation with  
880 Permian magmatism at  $254 \pm 16$  Ma. SA, Sidi Ahmed; IA, Ighrem Aousser; S18, Structure 18; FN,  
881 Filons Nord; F.P, Filons Parallèles.

882

883

884 **Table captions**

885 **Table 1.** REE pattern of gangue carbonate from the different Pb-Zn-Ag veins.

886 **Table 1.** C-O isotopic compositions of gangue carbonates from the Pb-Zn-Ag ore. C-O isotopic  
887 compositions of the fluid in equilibrium with gangue carbonates have been calculated using Zheng  
888 (1999) and Chacko et al. (1991) thermometers.

889 **Table 3.** Sm and Nd contents and  $\epsilon_{Nd}$  of the gangue carbonates from the Pb-Zn-Ag deposit of Tighza  
890 district.

891 **Table 4.** Noble gas compositions of fluids trapped in sulphide minerals from the Tighza polymetallic  
892 district.

893 **Table 5.** Pb-Pb isotopic ratios of galena.

894

Table 1. REE contents (ppm) in the carbonates from the Tighza district. Mineral abbreviations from Kretz (1983).

	Paralleles veins			Nord vein	Signal vein	Sidi Ahmed vein						Ighrem Aousser vein										
	Tz11/13.2	Tz11/10	Tz11/13.1	Tz11/67	Tz11/47	Tz10/22	Tz10/17	Tz11/49	Tz11/48	Tz10/25	Tz11/53	Tz10/30.2	Tz10/33	Tz10/33	Tz10/30.1	Tz10/31	Tz10/28	Tz10/29	Tz11/58	Tz10/32	Tz10/34	Tz10/31
	sid	ank	ank	ank	P1 sid	P1 sid	P2 ank	P4 cal	P4 cal	P4 cal	P4 cal	P2 ankérite	P2 ankérite	P3 sidérite	P4 calcite	P4 calcite	P4 calcite	P4 calcite	P4 calcite	P4 calcite	P4 calcite	P4 calcite
<b>La</b>	6.67	11.22	12.34	11.19	95.94	32.52	14.75	105.20	47.60	107.50	36.23	665.60	12.87	5.22	140.10	132.30	61.47	127.60	38.27	448.40	133.20	322.80
<b>Ce</b>	17.72	56.70	60.37	45.51	174.60	65.15	59.83	138.60	83.85	218.10	61.61	1352.00	49.75	13.75	279.00	282.80	138.10	266.20	62.26	1020.00	275.90	727.00
<b>Pr</b>	2.72	11.45	11.74	8.35	20.42	7.97	9.70	15.29	9.59	28.24	7.19	174.00	8.07	1.92	34.41	36.43	18.74	33.40	6.84	132.40	35.02	92.76
<b>Nd</b>	11.44	55.42	54.99	38.87	87.39	34.63	45.42	65.08	45.58	132.80	34.24	742.70	43.61	9.95	147.60	159.50	91.33	142.40	33.74	538.80	151.90	372.60
<b>Sm</b>	3.64	26.27	24.46	16.19	22.50	9.63	19.31	16.01	13.97	35.53	9.71	262.10	19.50	3.31	44.79	54.37	27.39	41.76	9.17	158.60	50.46	112.00
<b>Eu</b>	1.74	11.99	13.09	7.79	7.98	5.13	6.47	6.66	5.98	4.76	4.22	152.80	8.35	1.89	23.94	29.74	3.01	21.17	5.18	55.98	27.57	42.85
<b>Gd</b>	3.39	25.21	23.61	15.87	21.30	9.07	19.39	20.77	15.17	41.16	10.42	306.70	20.17	3.20	48.24	60.42	34.70	43.15	11.55	162.40	55.69	113.50
<b>Tb</b>	0.52	3.66	3.40	2.18	2.96	1.20	2.63	2.40	2.25	6.65	1.48	41.91	2.73	0.48	7.11	8.41	6.54	6.11	1.57	22.01	8.09	15.29
<b>Dy</b>	2.69	17.44	16.13	10.12	15.69	5.88	11.89	11.11	11.33	41.06	7.30	196.60	12.15	2.41	37.19	40.39	46.54	30.01	7.76	99.44	40.57	66.53
<b>Ho</b>	0.46	2.61	2.41	1.48	2.87	0.96	1.64	1.84	1.87	8.49	1.22	29.08	1.70	0.38	6.27	6.14	11.21	4.87	1.28	13.96	6.57	9.08
<b>Er</b>	1.16	5.94	5.44	3.22	8.60	2.39	3.44	4.27	4.82	23.29	3.04	62.53	3.61	0.92	15.97	14.13	38.44	12.17	3.01	27.83	16.19	18.12
<b>Tm</b>	0.17	0.77	0.71	0.40	1.70	0.36	0.43	0.51	0.69	3.14	0.40	7.37	0.44	0.13	2.33	1.83	7.14	1.68	0.36	2.97	2.29	2.01
<b>Yb</b>	1.19	5.06	4.68	2.61	17.18	2.58	2.79	3.13	4.76	18.84	2.53	42.71	2.88	0.92	16.36	12.65	59.08	11.54	1.98	17.28	16.21	12.88
<b>Lu</b>	0.17	0.71	0.65	0.35	3.22	0.37	0.38	0.48	0.72	2.50	0.36	5.40	0.40	0.13	2.40	1.77	10.13	1.75	0.27	2.30	2.40	1.86
<b>Y</b>	13.31	76.59	70.07	50.44	81.69	28.89	58.38	93.59	64.59	307.8	43.03	1117	57.65	11.83	230.3	239.2	430.2	202.6	50.46	545.5	239.7	391.6
<b>ΣREE</b>	54	234	234	164	482	178	198	391	248	672	180	4041	186	45	806	841	554	744	183	2702	822	1909
<b>Eu/Eu*</b>	2.34	2.19	2.56	2.29	1.72	2.59	1.57	1.72	1.93	0.59	1.98	2.54	1.98	2.73	2.43	2.44	0.46	2.35	2.37	1.64	2.45	1.79
<b>(La/Yb)<sub>N</sub></b>	0.41	0.16	0.19	0.32	0.41	0.93	0.39	2.48	0.74	0.42	1.06	1.15	0.33	0.42	0.63	0.77	0.08	0.82	1.43	1.92	0.61	1.85
<b>ΣREE+Y</b>	67	311	304	215	564	207	256	485	313	980	223	5158	244	56	1036	1080	984	946	234	3248	1062	2301
<b>% Y</b>	19.9	24.6	23.0	23.5	14.5	14.0	22.8	19.3	20.7	31.4	19.3	21.7	23.6	21.0	22.2	22.1	43.7	21.4	21.6	16.8	22.6	17.0
<b>% Ce</b>	26.5	18.2	19.9	21.2	31.0	31.5	23.3	28.6	26.8	22.3	27.6	26.2	20.4	24.4	26.9	26.2	14.0	28.1	26.6	31.4	26.0	31.6
<b>% Nd</b>	17.1	17.8	18.1	18.1	15.5	16.8	17.7	13.4	14.6	13.6	15.4	14.4	17.9	17.6	14.2	14.8	9.3	15.0	14.4	16.6	14.3	16.2
<b>% La</b>	10.0	3.6	4.1	5.2	17.0	15.7	5.8	21.7	15.2	11.0	16.2	12.9	5.3	9.2	13.5	12.2	6.2	13.5	16.4	13.8	12.5	14.0
<b>%REE+Y</b>	73.4	64.3	65.0	68.0	77.9	78.0	69.6	83.0	77.3	78.2	78.5	75.2	67.2	72.2	76.9	75.3	73.3	78.1	79.0	78.6	75.4	78.8

Table 2. C-O isotopic compositions of gangue carbonates from the Pb-Zn-Ag ore. C-O isotopic compositions of the fluid in equilibrium with the carbonate have been calculated using Zheng (1999) and Chacko et al. (1991) thermometers.

Stage	Mineral	Sample	$\delta^{18}\text{O}_{\text{SMOW}}$	$\delta^{13}\text{C}_{\text{PDB}}$	$\delta^{18}\text{O}_{\text{SMOW}}$	$\delta^{13}\text{C}_{\text{PDB}}$	$\delta^{18}\text{O}_{\text{SMOW}}$	$\delta^{13}\text{C}_{\text{PDB}}$
					T = 230°C	T = 230°C	T = 280°C	T = 280°C
<b>Sidi Ahmed vein</b>								
P1	siderite	Tz10/23	21,3	-5,1	11.9	-3.6	14.0	-2.6
P1	siderite	Tz10/22	21,1	-4,2	11.8	-2.6	13.8	-1.6
P2	ankerite	Tz10/18	21,9	-3,6	13.1	-2.1	15.0	-1.0
P2	ankerite	Tz10/23	24,0	-5,0	15.1	-3.4	17.1	-2.4
P2	ankerite	Tz10/17	19,2	-4,0	10.4	-2.4	12.4	-1.4
P2	ankerite	Tz10/36	20,2	-3,7	11.4	-2.2	13.4	-1.2
P2	ankerite	Tz11/49	21,6	-11,2	13.3	-9.6	15.2	-8.6
P3	siderite	Tz10/18	21,5	-4,5	12.1	-3.0	14.2	-2.0
P4	calcite	Tz11/53	20,3	-8,3	12.0	-6.7	13.9	-5.7
P4	calcite	Tz11/49	22,0	-8,7	13.7	-7.2	15.6	-6.2
P4	calcite	Tz10/25	11,9	-5,7	3.6	-4.1	5.5	-3.1
<b>Ighrem Aousser vein</b>								
P1	siderite	Tz10/29	19,1	-4,5	9.7	-3.0	11.8	-2.0
P2	ankerite	Tz10/30	23,0	-4,1	14.2	-2.6	16.2	-1.6
P2	ankerite	Tz10/33	20,9	-3,8	12.0	-2.3	14.0	-1.3
P3	siderite	Tz10/33	21,4	-4,7	12.1	-3.2	14.2	-2.2
P4	calcite	Tz10/29	20,0	-6,2	11.7	-4.7	13.6	-3.7
P4	calcite	Tz10/31	20,1	-6,2	11.8	-4.7	13.7	-3.7
P4	calcite	Tz10/32	20,3	-6,0	12.0	-4.4	13.9	-3.4
P4	calcite	Tz10/34	19,5	-6,4	11.2	-4.8	13.1	-3.8
P4	calcite	Tz11/58	21,0	-7,3	12.7	-5.8	14.6	-4.8
<b>Signal vein</b>								
P1	siderite	Tz12/01	20,4	-5,1	11.1	-3.6	13.2	-2.6
P2	ankerite	Tz12/02	24,2	-5,3	15.3	-3.8	17.3	-2.7
P4	calcite	Tz10/09	19,0	-2,5	10.7	-1.0	12.6	0.1
P4	calcite	Tz12/01	16,1	-5,8	7.8	-4.3	9.7	-3.2

Table 3. Sm and Nd contents and  $\epsilon\text{Nd}$  of the gangue carbonates from the Pb-Zn-Ag deposit of Tighza district.

Stage	Mineral	Sample	[Nd] ppm	[Sm] ppm	$^{143}\text{Nd}/^{144}\text{Nd}$ ( $2\sigma$ ) <sup>a</sup>	$^{147}\text{Sm}/^{144}\text{Nd}$	$\epsilon\text{Nd}_0$	$(^{143}\text{Nd}/^{144}\text{Nd})_{255\text{Ma}}$ <sup>b</sup>	$\epsilon\text{Nd}_{255\text{Ma}}$ <sup>b</sup>	% basement
<b>Sidi Ahmed vein</b>										
P2	ankerite	Tz10/17	30.64	11.94	0.512370 (5)	0.2353	-5.23	0.511977	-6.49	0.53
P2	ankerite	Tz10/22	31.08	8.26	0.512256 (10)	0.1604	-7.45	0.511988	-6.28	0.50
P2	ankerite	Tz11/49	67.11	15.78	0.512201 (2)	0.1419	-8.53	0.511964	-6.76	0.56
P3	calcite	Tz10/25	80.98	23.96	0.512221 (4)	0.1785	-8.14	0.511923	-7.56	0.66
P3	calcite	Tz11/48	46.48	13.55	0.512197 (2)	0.1759	-8.61	0.511903	-7.94	0.71
P3	calcite	Tz11/53	170.91	49.24	0.512246 (4)	0.1739	-7.65	0.511956	-6.91	0.58
<b>Ighrem Aousser vein</b>										
P2	ankerite	Tz10/30.2	303.16	112.91	0.512390 (3)	0.2247	-4.84	0.512015	-5.76	0.44
P2	ankerite	Tz10/31	154.32	48.90	0.512252 (3)	0.1912	-7.53	0.511933	-7.36	0.64
P2	ankerite	Tz10/33.1	8.90	3.14	0.512343 (17)	0.2127	-5.76	0.511988	-6.28	0.50
P2	siderite	Tz10/33.2	42.58	17.87	0.512374 (5)	0.2532	-5.15	0.511951	-7.00	0.59
P3	calcite	Tz11/58	31.98	8.48	0.512206 (3)	0.1601	-8.43	0.511939	-7.24	0.62
P3	calcite	Tz10/28	114.00	26.09	0.512176 (3)	0.1381	-9.01	0.511946	-7.11	0.61
P3	calcite	Tz10/29	130.39	41.51	0.512246 (3)	0.1921	-7.66	0.511925	-7.51	0.66

<sup>a</sup> The figures in parentheses refer to uncertainties of the measurements on the last decimals.

<sup>b</sup>  $\epsilon\text{Nd}_0$  refers to present day;  $\epsilon\text{Nd}_{255\text{Ma}}$  calculated at the age of the Pb-Zn-Ag formation (Rossi et al., 2016) using the following present-day values for CHUR:  $^{147}\text{Sm}/^{144}\text{Nd}=0.1966$  and  $^{143}\text{Nd}/^{144}\text{Nd}=0.512638$  (Jacobsen and Wasserburg, 1980).

Table 4. Noble gas compositions of fluids trapped in sulphide minerals from the Tighza polymetallic district.

	mineral	vein	mass g	He x 10 <sup>-12</sup> mol/g	<sup>3</sup> He/ <sup>4</sup> He	<sup>40</sup> Ar x 10 <sup>-12</sup> mol/g	<sup>40</sup> Ar/ <sup>36</sup> Ar	<sup>38</sup> Ar/ <sup>36</sup> Ar
<b>W-Au</b>								
Tz11/23	As-pyrite	W1N	0.500	7.41 ± 0.107	1.814 ± 0.097	7.33 ± 0.286	256 ± 10	0.189 ± 0.013
Tz10/07	As-pyrite	Signal	0.300	8.17 ± 0.117	1.083 ± 0.069	4.08 ± 0.166	304 ± 12	0.181 ± 0.012
Tz10/01	Pyrite	W1N	0.400	4.61 ± 0.069	1.658 ± 0.053	8.77 ± 0.215	328 ± 13	0.168 ± 0.012
<b>Pb-Zn-Ag</b>								
Tz11/35	Pyrite	Sidi Ahmed	0.305	16.3 ± 0.240	0.054 ± 0.005	20.2 ± 0.400	315 ± 12	0.180 ± 0.012
Tz10/53	Pyrite	Sidi Ahmed	0.423	1.42 ± 0.021	0.018 ± 0.012	2.67 ± 0.125	299 ± 12	0.187 ± 0.013
Tz10/54	Sphalérite	Sidi Ahmed	0.414	7.81 ± 0.112	0.103 ± 0.011	19.6 ± 0.750	284 ± 11	0.185 ± 0.013

Table 5. Pb-Pb isotopic ratios of galena.

galènes	$^{206}\text{Pb}/^{204}\text{Pb}$	$\pm 2\sigma$	$^{207}\text{Pb}/^{204}\text{Pb}$	$\pm 2\sigma$	$^{208}\text{Pb}/^{204}\text{Pb}$	$\pm 2\sigma$
<i>Ighrem Aousser vein (3F)</i>						
Tz10.30_1	18,14	0,03	15,54	0,03	37,74	0,09
Tz10.30_4	18,13	0,02	15,54	0,02	37,78	0,06
Tz10.30_5	18,13	0,02	15,54	0,02	37,78	0,07
Tz10.30_6	18,16	0,02	15,56	0,02	37,60	0,05
Tz10.30_7	18,20	0,01	15,62	0,01	37,50	0,03
<i>Sidi Ahmed vein (1270)</i>						
Tz10-31_8	18,23	0,01	15,57	0,01	38,34	0,03
Tz10-31_9	18,26	0,01	15,62	0,01	38,47	0,02
Tz10-31_10	18,27	0,02	15,57	0,03	38,42	0,04
Tz10-35_27	18,50	0,01	15,79	0,01	39,47	0,01
Tz10-35_29	18,40	0,02	15,72	0,02	39,10	0,05
Tz10-35_30	18,43	0,01	15,72	0,01	39,19	0,02
Tz10-35_31	18,38	0,01	15,69	0,01	39,10	0,02
Tz10-35_33	18,41	0,01	15,72	0,01	39,16	0,02
Tz10-35_34	18,47	0,01	15,75	0,01	39,42	0,03
<i>Signal vein(1270)</i>						
Tz10-39_21	18,46	0,010	15,71	0,01	39,30	0,04
Tz10-39_23	18,38	0,016	15,68	0,01	39,08	0,04
Tz10-39_24	18,42	0,019	15,70	0,02	39,11	0,06
Tz11_42Bgal@11	18,127	0,007	15,48	0,01	38,089	0,01
Tz11_42Bgal@12	18,121	0,009	15,48	0,01	38,054	0,02
Tz11_42Bgal@13	18,122	0,007	15,48	0,01	38,089	0,01
Tz11_42Bgal@14	18,152	0,009	15,51	0,01	38,147	0,02
Tz11_42Bgal@15	18,14	0,009	15,51	0,01	38,141	0,02
Tz11_42Bgal@16	18,16	0,007	15,51	0,01	38,182	0,02
Tz11_42Bgal@17	18,14	0,008	15,49	0,01	38,14	0,02
Tz11_42Bgal@18	18,133	0,007	15,50	0,01	38,137	0,02
Tz11_42Bgal@19	18,137	0,007	15,51	0,01	38,15	0,02
Tz11_42Bgal@20	18,127	0,007	15,49	0,01	38,118	0,02
Tz11_42Bgal@21	18,125	0,007	15,49	0,01	38,104	0,02
Tz11_42Bgal@22	18,113	0,007	15,48	0,01	38,094	0,01
Tz11_42Bgal@23	18,127	0,006	15,49	0,01	38,114	0,01
Tz11_42Bgal@24	18,142	0,007	15,50	0,01	38,158	0,01
Tz11_42Bgal@25	18,125	0,006	15,48	0,01	38,081	0,01
Tz11_42Bgal@26	18,129	0,009	15,49	0,01	38,096	0,02
Tz11_42Bgal@27	18,163	0,018	15,55	0,03	38,285	0,10
Tz11_42Bgal@28	18,044	0,015	15,40	0,01	37,746	0,03
Tz11_42Bgal@29	18,082	0,016	15,43	0,01	37,752	0,04
Tz11_42Bgal@30	18,091	0,016	15,43	0,01	37,767	0,03
Tz11_42Bgal@31	18,084	0,011	15,42	0,01	37,73	0,02
Tz11_42Bgal@32	18,081	0,014	15,41	0,01	37,747	0,03
Tz11_42Bgal@33	18,055	0,012	15,40	0,01	37,74	0,02
Tz11_42Bgal@34	18,077	0,013	15,42	0,01	37,768	0,03
Tz11_42Bgal@35	18,06	0,012	15,41	0,01	37,752	0,03



Tz10-43_12	18,23	0,012	15,58	0,01	38,37	0,03
Tz10-43_17	18,39	0,015	15,68	0,01	39,01	0,03
Tz10-43_18	18,40	0,013	15,73	0,01	39,12	0,03
Tz10-43_20	18,44	0,007	15,73	0,01	39,28	0,02

---

ACCEPTED MANUSCRIPT

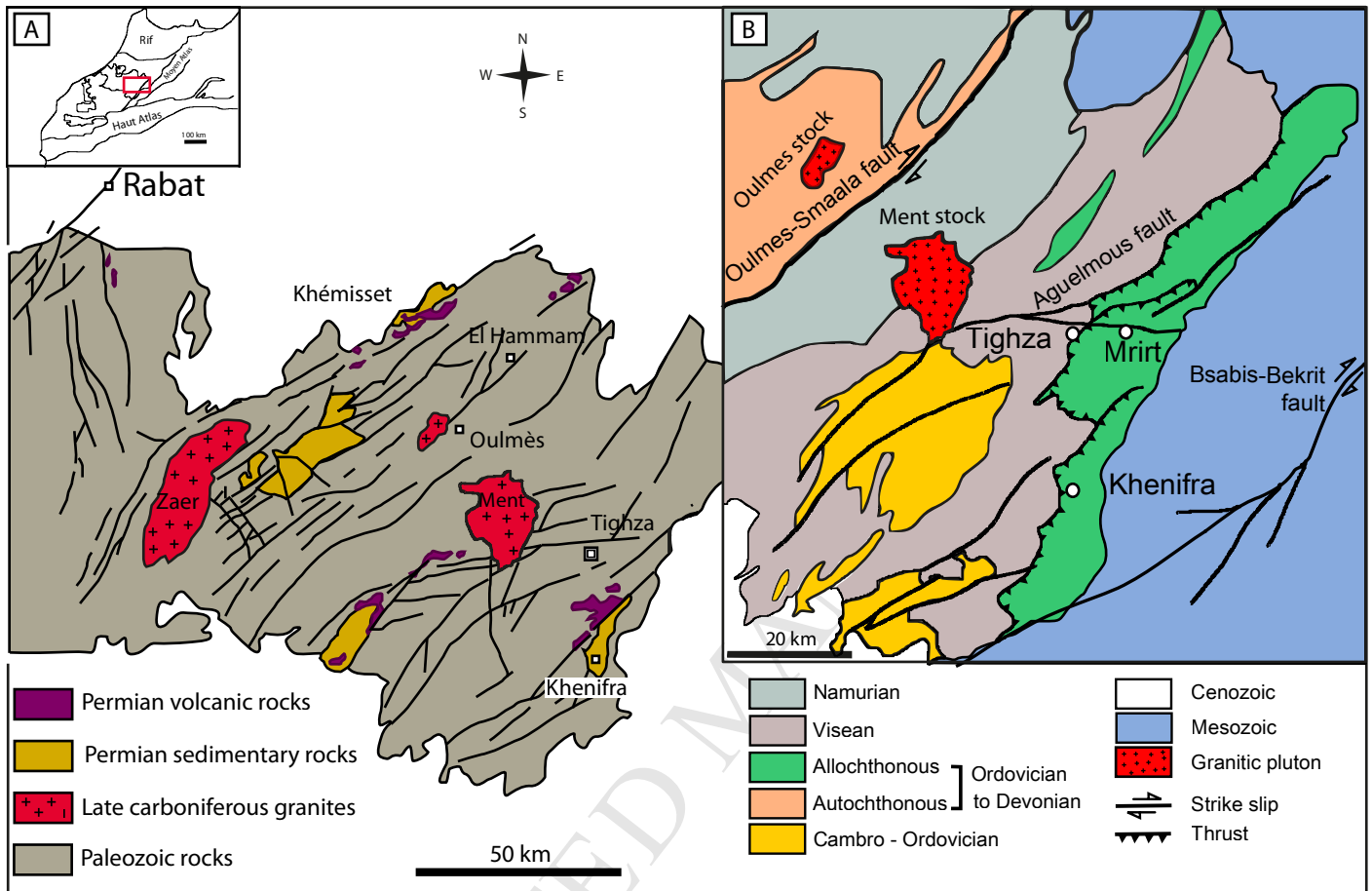


Figure 1

Rossi et al.

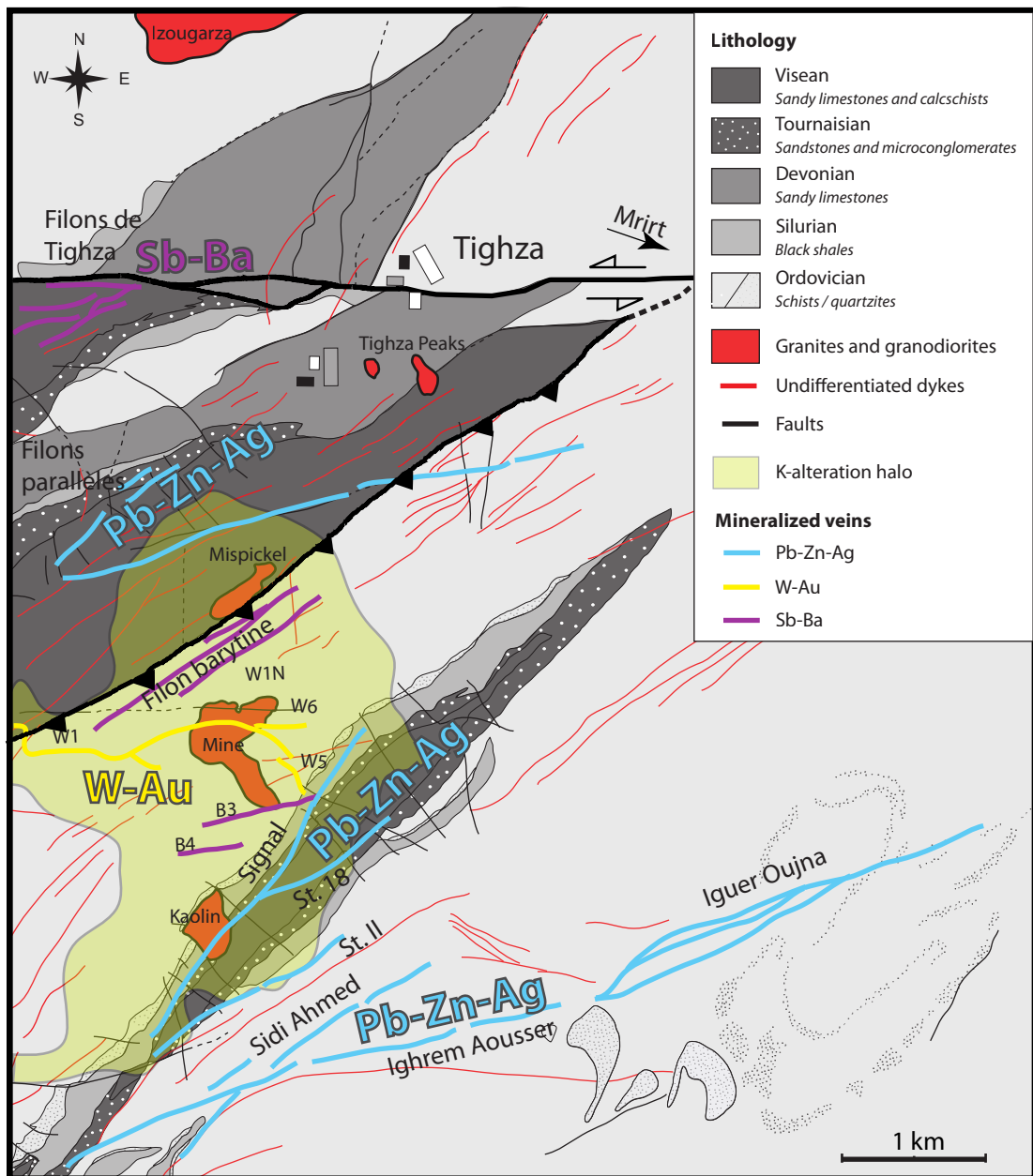


Figure 2

Rossi et al.

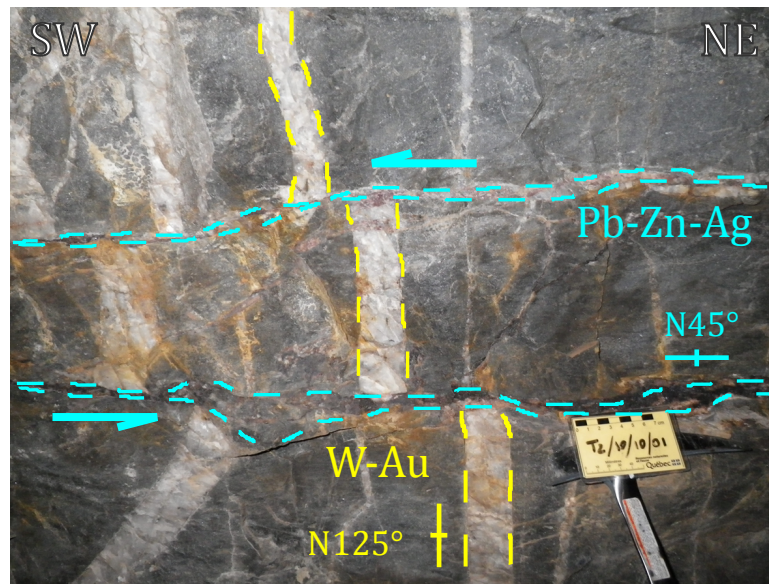


Figure 3

Rossi et al.

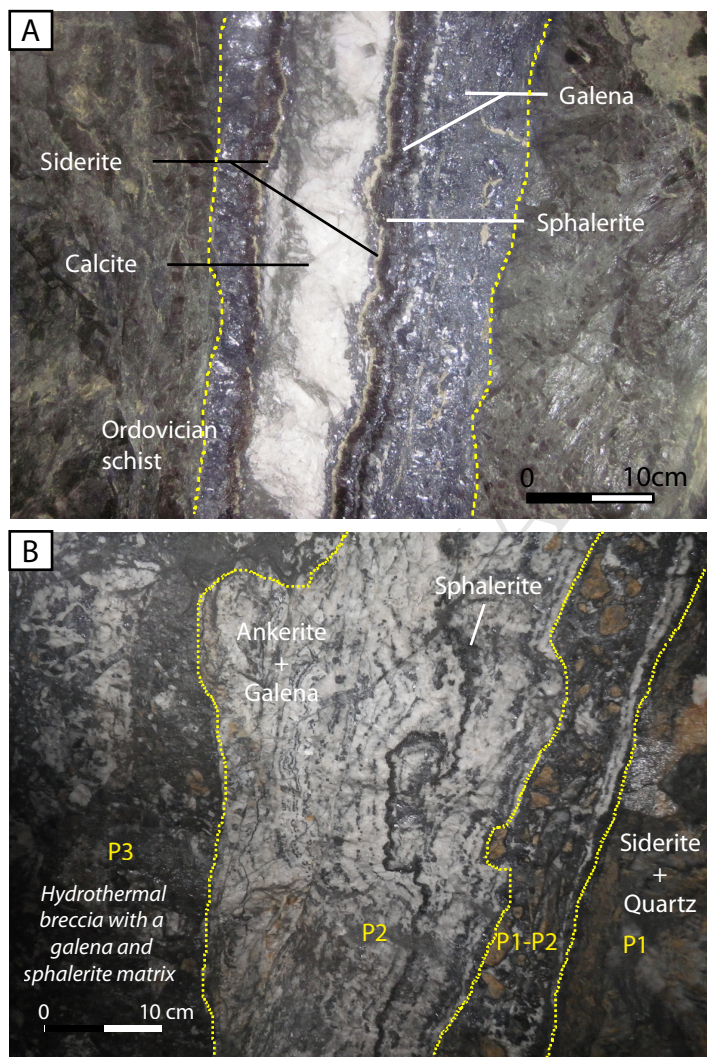


Figure 4

Rossi et al.

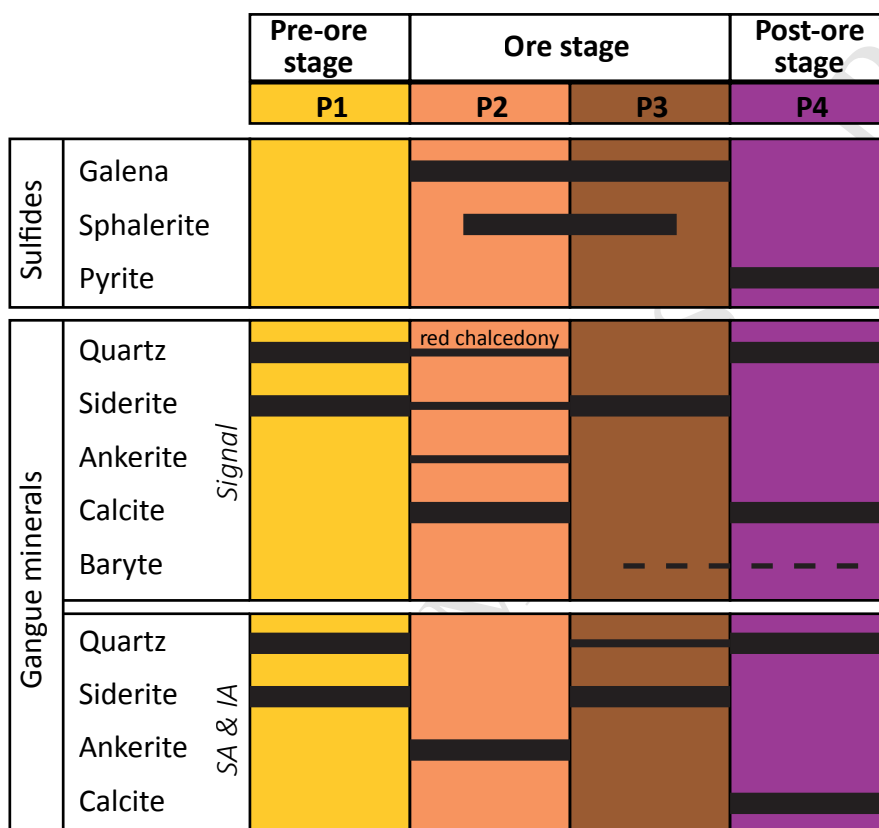


Figure 5

Rossi et al.

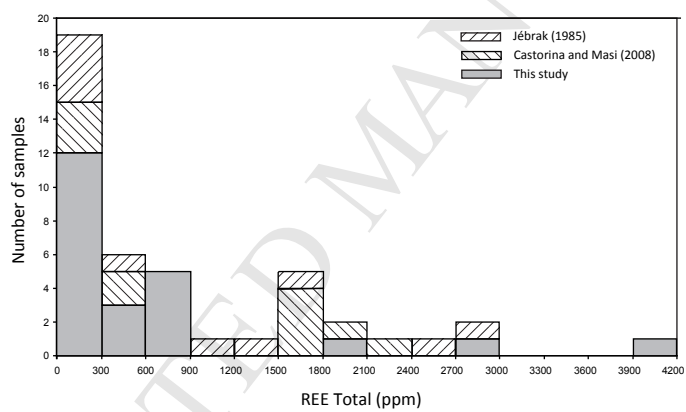


Figure 6

Rossi et al.

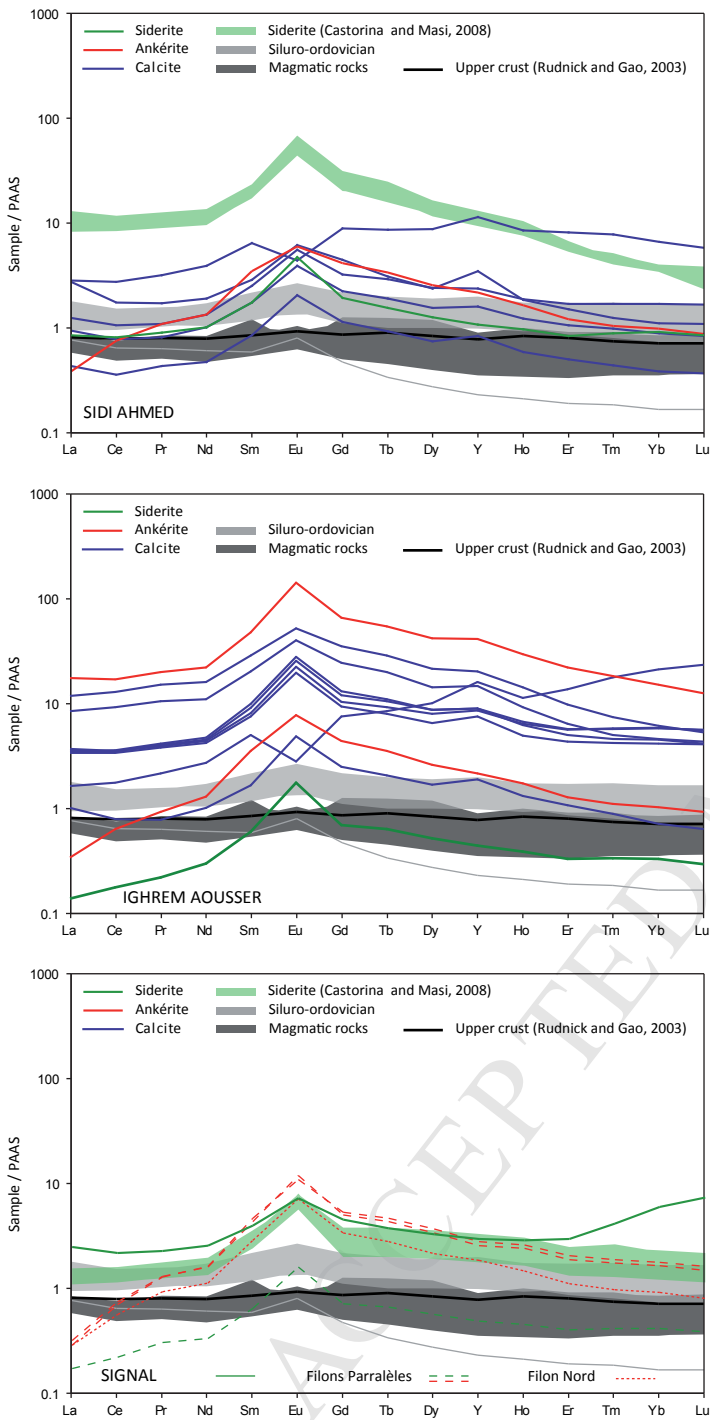


Figure 7

Rossi et al.



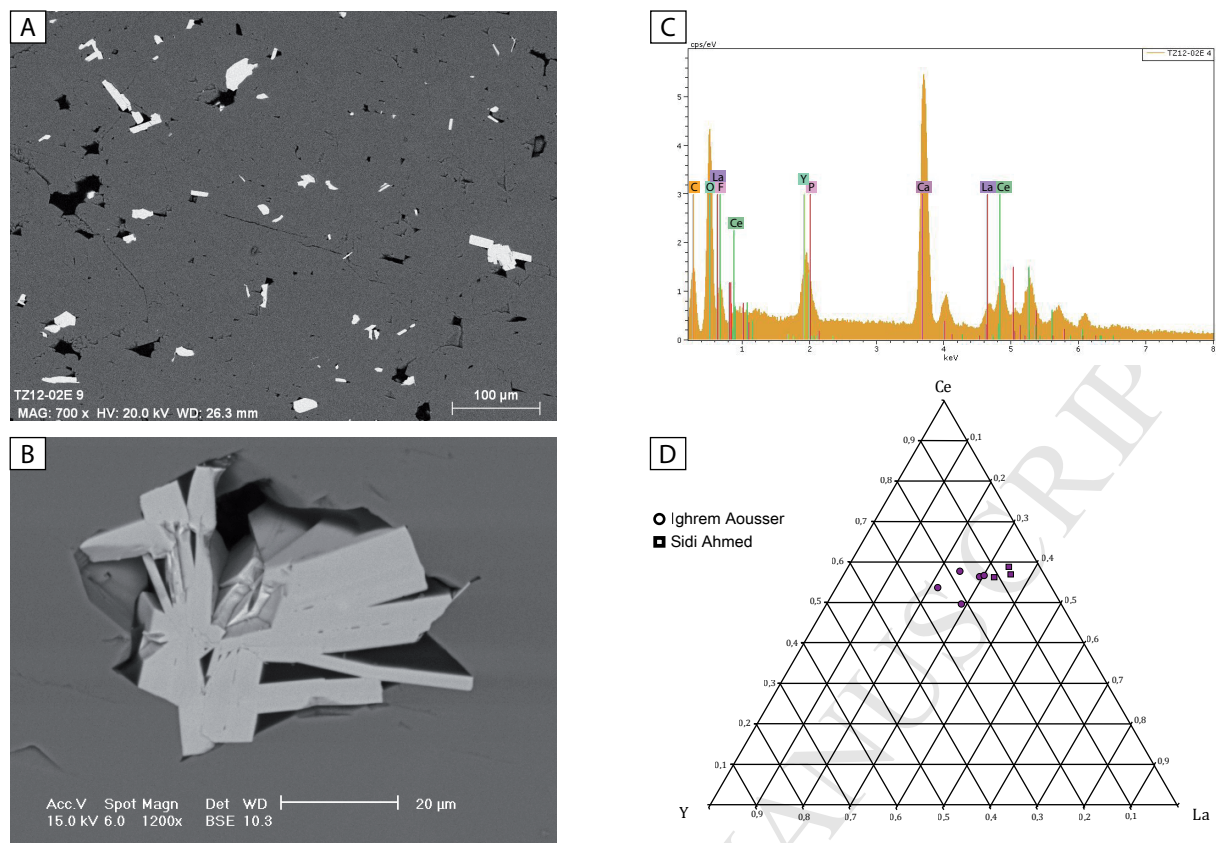


Figure 8

Rossi et al.

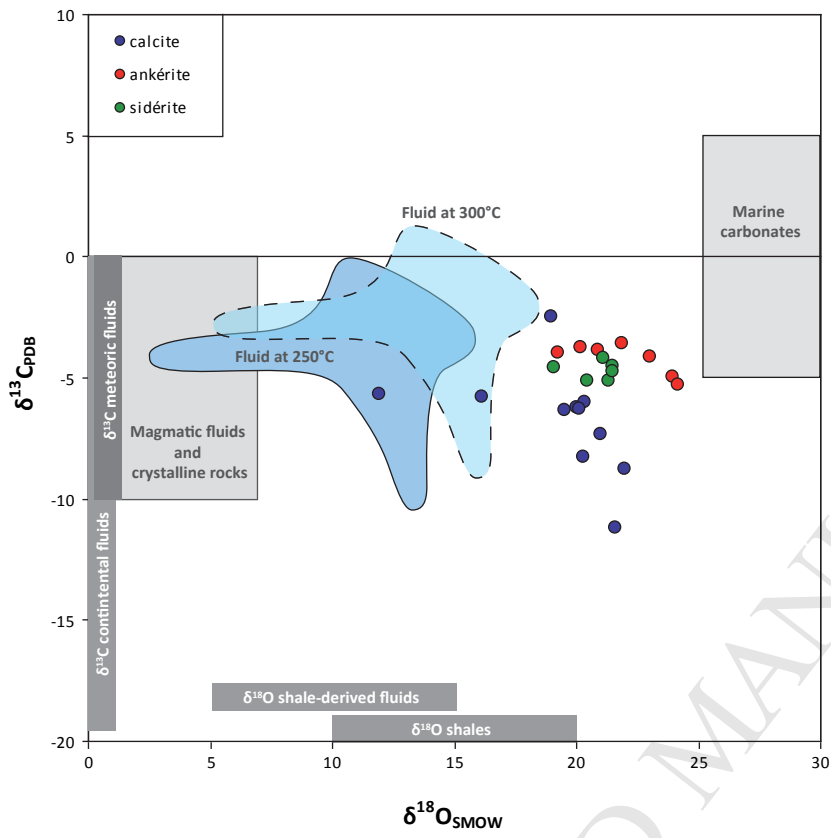


Figure 9

Rossi et al.

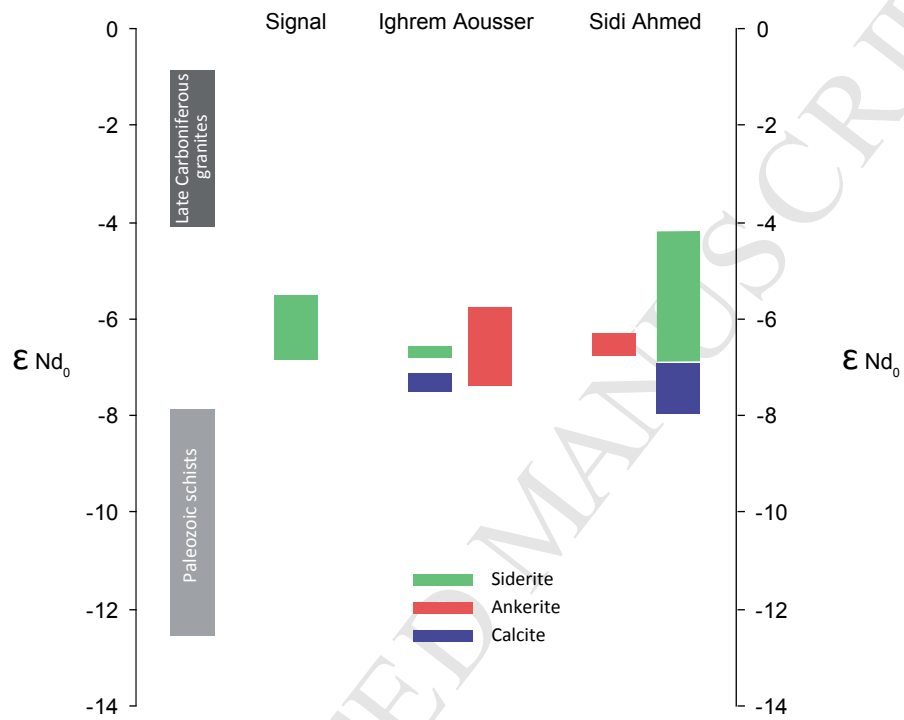


Figure 10

Rossi et al.

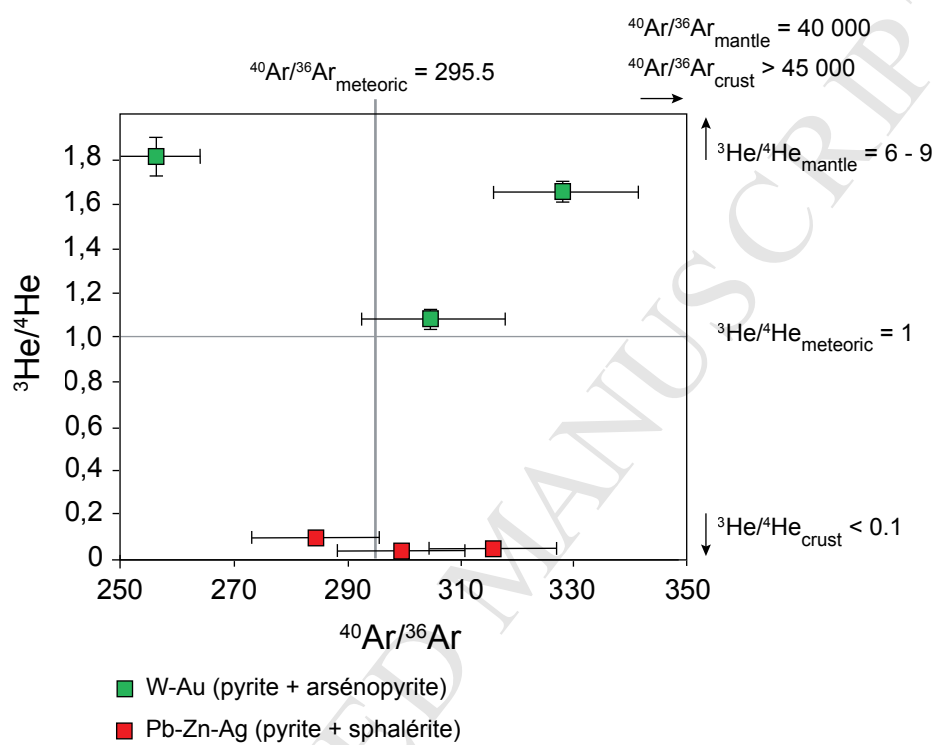


Figure 11

Rossi et al.

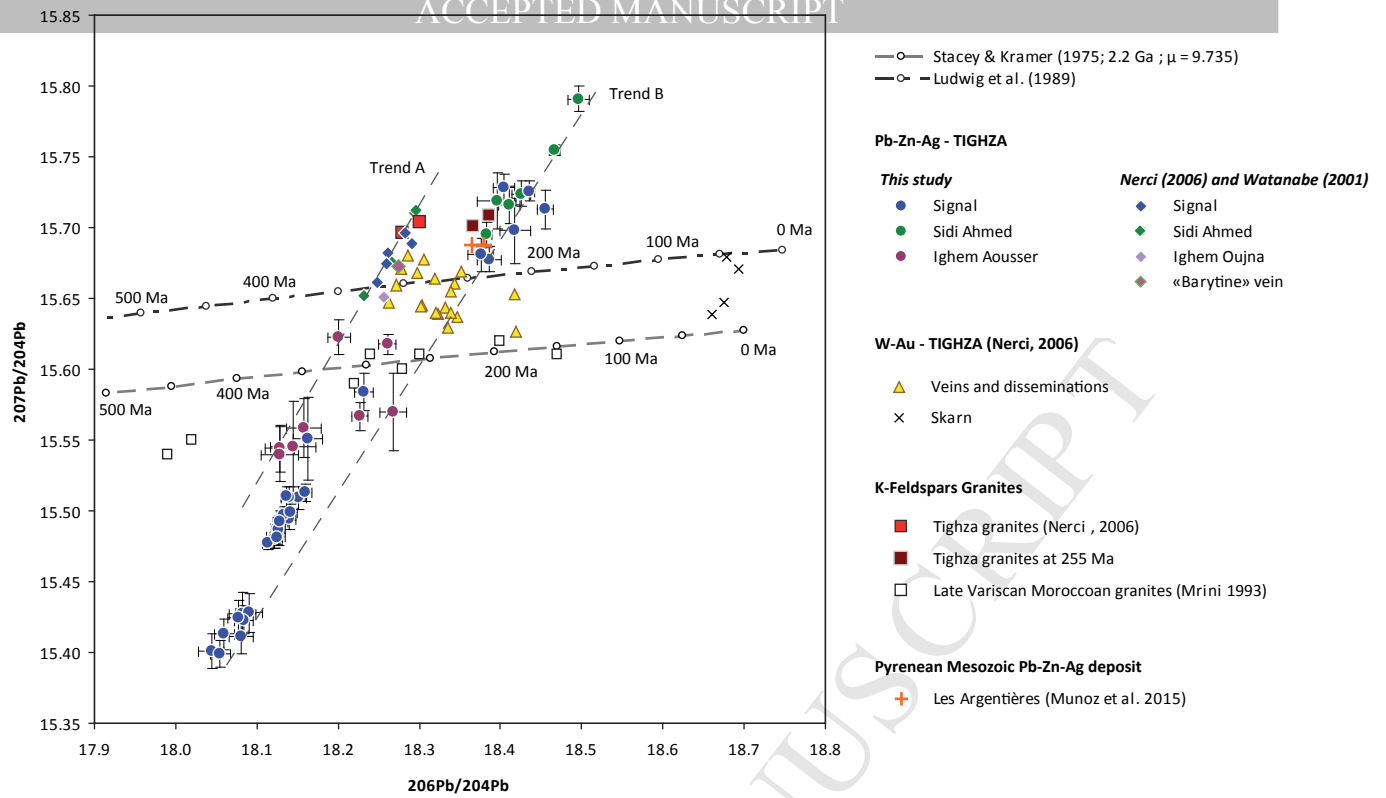


Figure 12

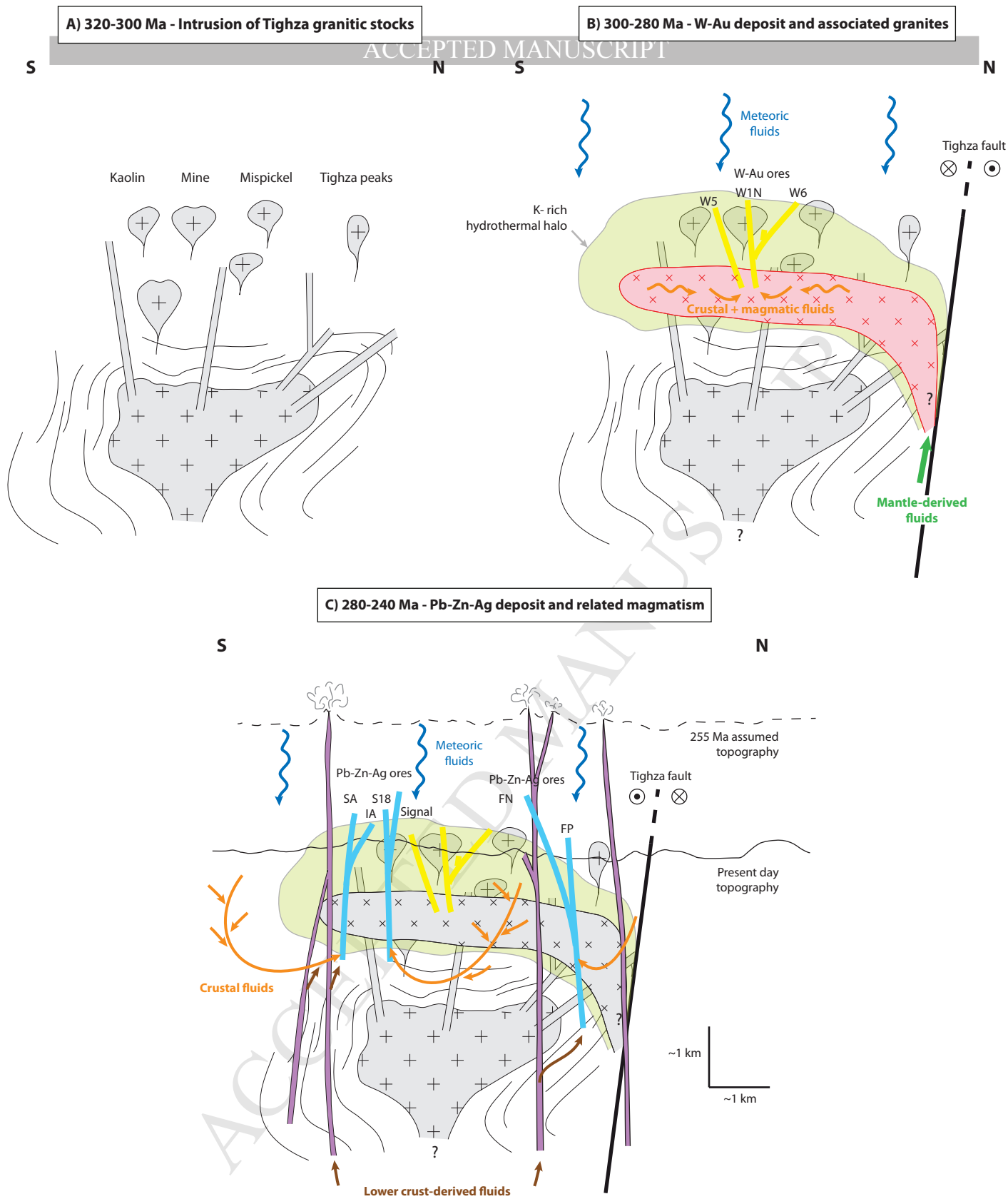


Figure 13

Rossi et al.

## Highlights Rossi et al. JAES

- Pb-Zn-Ag vein-type mineralization disconnected from adjacent late-Variscan granites
- Epithermal Pb-Zn-Ag veins related to Permo-Triassic extension and magmatic activity
- Complex hydrothermal system resulting from mixing various crustal fluids
- A new metallogenic model for Pb-Zn-Ag veins and new exploration guides